THE JOURNAL OF
PHYSICAL CHEMISTRY C
Article
pubs.acs.org/JPCC

Plasmons in Molecules

Stephan Bernadotte,[†] Ferdinand Evers,[‡,§,*] and Christoph R. Jacob*[,†]

[†]Center for Functional Nanostructures and Institute of Physical Chemistry, Karlsruhe Institute of Technology (KIT), Wolfgang-Gaede-Strasse 1a, 76131 Karlsruhe, Germany

[‡]Institute of Nanotechnology, Karlsruhe Institute of Technology (KIT), Hermann-von-Helmholtz-Platz 1, 76344 Eggenstein-Leopoldshafen, Germany

[§]Institut für Theorie der Kondensierten Materie, Karlsruhe Institute of Technology (KIT), Wolfgang-Gaede-Strasse 1, 76131 Karlsruhe, Germany

ABSTRACT: The classification of electronic excitations in molecules and molecular nanostructures plays an important role when tailoring materials with desired properties. One example of such a class of excitations are plasmons. Plasmons appear in solid-state physics, where they are characterized as density oscillations in an electron gas that are driven by the restoring forces associated with the electromagnetic field induced by the density oscillations themselves. Here, we investigate how this concept can be transferred to molecular systems by performing a step-by-step analysis, starting from three-dimensional bulk systems and ending with molecules. On the basis of this analysis, we propose to scale the electron−electron interaction in quantum-chemical response calculations in order to identify plasmons in molecules. This approach is illustrated for molecular chains and clusters. Our results show that the concept of plasmons is still applicable for extended molecular systems and demonstrate that the proposed scaling approach provides an easy way of characterizing electronic excitations.

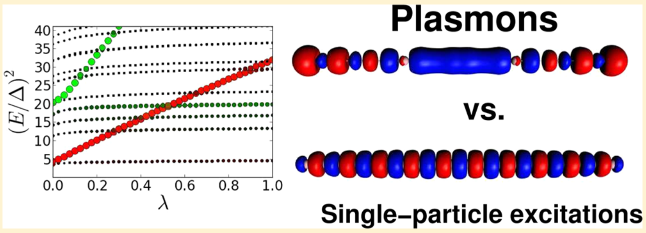

1. INTRODUCTION

The optical properties of nanostructured materials and nanoclusters are determined by their electronically excited states. Tailoring these optical properties for applications ranging from chemical and biological sensing[1−3] over solar energy conversion[4,5] to the fabrication of metamaterials[6−9] is the goal of "plasmonics", which has emerged as an important research field at the interface of physics, chemistry, and material science in the past decades.

The quantum-chemical description of the electronic excitations underlying such applications can be instructive both for the interpretation of experiments and for designing new materials.[10] However, the accurate treatment of electronic excitations relevant in plasmonics presents a challenge. First, for excited states it is usually more difficult than for the ground state to calculate their properties with the accuracy required for a meaningful comparison with experiment.[11−13] Second, the size of the nanoclusters of interest poses an additional difficulty.[14] Not only does the computational demand increase with the size of the system, but also a larger number of excited states appear in the relevant energy range. Without a suitable classification of these electronic excitations this hampers the interpretation of the computational results and makes it difficult to identify the important excitations (for a discussion of this problem in the context of vibrational spectroscopy, see refs 15−17).

Of course, a classification of different types of electronic excitations is useful both for the interpretation of quantum-chemical calculations and for selectively targeting excitations that are of interest for predicting optical or other spectroscopic properties. Typically, the classification of electronic excitations within quantum chemistry is based on a rather technical approach,[11] and driven by the need to decide which quantum-chemical methods are appropriate for describing the excitations of interest.[12] For instance, one distinguishes valence and Rydberg excitations for determining whether asymptotically corrected exchange−correlation potentials are needed when using time-dependent density-functional theory (TDDFT)[18,19] and distinguishes charge-transfer and local excitations for deciding whether TDDFT with standard nonhybrid exchange−correlation functionals can be employed.[20,21]

An alternative route is chosen in solid-state physics where the electronic excitations in metallic systems are classified as single-particle excitations and plasmons.[22−24] The distinction of plasmons and single-particle excitations can be motivated from the homogeneous electron gas model.[23,25] Here, plasmons are collective charge density oscillations with a strong induced electromagnetic field, which provides a restoring force. These plasmonic excitations often determine the optical properties of metals, whereas the single-particle excitations play a role, e.g., in damping processes. Plasmons in extended systems are usually well-described by classical electrodynamics.[24,26]

These classical models can also be applied to nanosystems, such as metal clusters. For larger metal clusters, they usually

Received: November 15, 2012
Revised: December 20, 2012
Published: January 22, 2013

provide a rather accurate description of the optical spectrum[27−29] whereas extended models including quantum-mechanical corrections accounting for the presence of discrete energy levels can be used for more complicated cases.[30,31] For smaller clusters consisting of only tens to hundreds of atoms, classical models are no longer applicable and a full quantum-chemical treatment is usually necessary. In this case, the optical spectrum does not show a single strong plasmon peak anymore, but instead a spectrum with distinct peaks due to transitions between discrete energy levels is obtained, which is typical of molecular systems. When increasing the size of the clusters, the optical spectrum obtained from full quantum-chemical calculations approaches the one predicted by classical models.[32,33]

In such calculations a large number of electronic excitations contribute to the plasmon peak, and the distinction between plasmons and single-particle excitations present for the homogeneous electron gas is not immediately apparent anymore in standard quantum-chemical calculations. Therefore, it is not straightforward to connect such calculations to the classical models of plasmons and to identify the important plasmonic excitations. Alternatively, the emergence of plasmons in molecular chains and clusters has been studied by using explicitly time-dependent methods.[34−37] However, in this case the optical spectrum is obtained, but individual electronic excitations cannot be identified anymore. Thus, despite the wide use of the term “plasmons” in such molecular systems, it often remains unclear how plasmonic excitations differ from other types of electronic excitations. In fact, all excitations with large oscillator strengths calculated in metal clusters are often referred to as plasmons (see, e.g., refs 32, 33, and 38). Here, we close this gap. We present a detailed analysis showing how the concept of a plasmon can be transferred to molecular systems and propose an approach for identifying plasmonic excitations in quantum-chemical calculations for molecules.

This work is organized as follows. In Section 2 the plasmonic resonances of the three-dimensional homogeneous electron gas are introduced both in a classical picture and in the framework of (quantum-mechanical) linear response theory. In addition, the distinction of plasmons and single-particle resonances is discussed. Subsequently, the downscaling from a three-dimensional system to a molecular wire is carefully analyzed. This is followed by an analysis of the electronic excitations in a linear sodium chain in Section 3. On the basis of our analysis, we then propose an approach for distinguishing plasmons and single-particle excitations in Section 4. This is applied to molecular chains and clusters in Section 5 and Section 6, respectively. Finally, a summary and concluding remarks are given in Section 7.

2. PLASMONS: FROM PERIODIC TO MOLECULAR SYSTEMS

2.1. Phenomenological Description. In solid-state physics, plasmons are typically discussed in the context of metals as long wavelength charge-density oscillations induced by an external perturbation.[22,24] For a classical description, we consider a homogeneous electron gas with a homogeneous positively charged background in a three-dimensional (3D) cube of volume V. If an external electric field $\mathcal{E}_{\text{ext}}$ is applied, the electron gas exhibits a density response, which is given by a displacement of the electronic density against the background by a shift Δx. This induced density in return gives rise to an induced electric field acting as a restoring force F,

$$F = -4\pi e^2 \rho_0 \Delta x \tag{1}$$

where e is the electron charge and ρ_0 is the electron (particle) density. Here and in the following, we are using Gaussian units. Classically, the movement of the electrons can be described by Newton’s equation,

$$m\frac{\partial^2 \Delta x}{\partial t^2} + 4\pi e^2 \rho_0 \Delta x = -e\mathcal{E}_{\text{ext}} \tag{2}$$

where m is the (effective) electron mass. Thus, one finds that the system behaves like a driven harmonic oscillator. Such a driven harmonic oscillator has a resonance frequency at

$$\omega^2 = \frac{4\pi e^2 \rho_0}{m} \tag{3}$$

This resonance corresponds to a collective electronic excitation of the classical electron gas, in which all electrons move as one entity. Comparing with eq 1, we notice that this resonance frequency is determined by the restoring force caused by the induced electric field.

2.2. Quantum-Mechanical Description. As starting point for a microscopic treatment, one considers the induced density $\delta\rho(r,\omega)$ as a response to an external scalar potential $\Phi_{\text{ext}}(r,\omega)$ oscillating with angular frequency ω,

$$\delta\rho(\mathbf{r}, \omega) = \int \chi_{\text{ext}}(\mathbf{r}, \mathbf{r}', \omega)\Phi_{\text{ext}}(\mathbf{r}', \omega)\, \mathrm{d}^3r' \tag{4}$$

where the external density response function $\chi_{\text{ext}}(r,r',\omega)$ has been introduced. This external response function depends on the angular frequency ω of the perturbation and its poles correspond to electronic excitation energies. The induced density gives rise to an induced Hartree potential,

$$\Phi_{\text{ind}}(\mathbf{r}, \omega) = \int f_{\text{Coul}}(\mathbf{r} - \mathbf{r}')\delta\rho(\mathbf{r}', \omega)\, \mathrm{d}^3r' \tag{5}$$

where f_{Coul} is the Coulomb kernel,

$$f_{\text{Coul}}(\mathbf{r} - \mathbf{r}') = \frac{e}{|\mathbf{r} - \mathbf{r}'|} \tag{6}$$

The induced Hartree potential adds to the external potential, yielding the total potential

$$\Phi_{\text{tot}}(\mathbf{r}, \omega) = \Phi_{\text{ext}}(\mathbf{r}, \omega) + \Phi_{\text{ind}}(\mathbf{r}, \omega) \tag{7}$$

The response equation, eq 4, can then be recast in the form

$$\begin{aligned}\delta\rho(\mathbf{r}, \omega) &= \int \chi_{\text{ext}}(\mathbf{r}, \mathbf{r}', \omega)\Phi_{\text{ext}}(\mathbf{r}', \omega)\, \mathrm{d}^3r' \\ &= \int \chi_{\text{irr}}(\mathbf{r}, \mathbf{r}', \omega)\Phi_{\text{tot}}(\mathbf{r}', \omega)\, \mathrm{d}^3r'\end{aligned} \tag{8}$$

where we have introduced the irreducible response function $\chi_{\text{irr}}(r,r',\omega)$ describing the response of the electron density to the change in the total potential. After substituting eqs 7 and 5 into the right-hand side of the above expression and rearranging, we obtain an integral equation,

$$\int \varepsilon(\mathbf{r}, \mathbf{r}'', \omega)\chi_{\text{ext}}(\mathbf{r}'', \mathbf{r}', \omega)\, \mathrm{d}^3r'' = \chi_{\text{irr}}(\mathbf{r}, \mathbf{r}', \omega) \tag{9}$$

where we introduced the dielectric function,

$$\begin{aligned}\varepsilon(\mathbf{r}, \mathbf{r}'', \omega) &= \delta(\mathbf{r} - \mathbf{r}'') \\ &\quad - \int \chi_{\text{irr}}(\mathbf{r}, \mathbf{r}''', \omega) f_{\text{Coul}}(\mathbf{r}''' - \mathbf{r}'')\, \mathrm{d}^3r'''\end{aligned} \tag{10}$$

Defining the inverse dielectric function ε^{-1} via

$$\int \varepsilon^{-1}(\mathbf{r}, \mathbf{r}'', \omega)\varepsilon(\mathbf{r}'', \mathbf{r}', \omega)\, \mathrm{d}^3r'' = \delta(\mathbf{r} - \mathbf{r}') \tag{11}$$

one can solve for χ_{ext} and obtains

$$\chi_{\text{ext}}(\mathbf{r}, \mathbf{r}', \omega) = \int \varepsilon^{-1}(\mathbf{r}, \mathbf{r}'', \omega)\chi_{\text{irr}}(\mathbf{r}'', \mathbf{r}', \omega)\, \mathrm{d}^3r'' \tag{12}$$

To find the electronic excitations of the system, we have to determine the poles of the external response function χ_{ext}. Considering eq 12, one can naively identify two different ways in which poles can arise.[22,39] First, poles of χ_{ext} should appear for frequencies that correspond to poles of χ_{irr}. Second, poles of χ_{ext} could also arise if the dielectric function ε has a zero mode (i.e., an eigenvalue equal to zero) for a certain frequency, i.e., if

$$\int \varepsilon(\mathbf{r}, \mathbf{r}', \omega_{\text{plas}})\pi(\mathbf{r}', \omega_{\text{plas}})\, \mathrm{d}^3r' = 0 \tag{13}$$

for a nonzero $\pi(\mathbf{r}',\omega_{\text{plas}})$ at the frequency ω_{plas}.

This distinction allows for an attempt to classify electronic excitations: The first type (i.e., those originating from poles of χ_{irr}) will be called *single-particle excitations*, whereas the second type (i.e., those originating from zero modes of ε) will be labeled *plasmons*. Note that the dielectric function ε contains the bare Coulomb kernel f_{Coul} whereas the irreducible response function χ_{irr} can be expressed via a perturbation expansion in the screened Coulomb interaction and is independent of f_{Coul} in zeroth order. Thus, single-particle excitations and plasmons are distinguished by their different dependence on the Coulomb kernel.

Two remarks should be made here: First, we notice that because ε^{-1} depends on χ_{irr}, the frequencies of poles of χ_{irr} will not be exactly equal to those of poles of χ_{ext}, but the presence of f_{Coul} leads to a (usually small) shift. This can be seen by multiplying eq 9 by $(\omega - \omega_0)$ where ω_0 is a resonance frequency and solving for χ_{ext} in the same manner as in eq 12. Second, if a frequency for which ε has a zero-mode (i.e., a plasmonic excitation) is close to a pole of χ_{irr} (i.e., a single-particle excitation), these two types of excitations will mix if they do not have different symmetries. Thus, in this case the separation of the electronic excitations (i.e., the poles of χ_{ext}) into plasmons and single-particle excitations may break down.

2.3. Random-Phase Approximation.

The linear-response formalism presented in the previous section can be employed for the (quantum-mechanical) calculation of the excitation energies. The simplest ansatz for the ground-state electronic wave function is a Slater determinant with single-particle orbitals $\{\phi_p\}$. The corresponding orbital energies are denoted as ε_p. The electrons occupy the lowest states according to the aufbau principle. Using the common quantum-chemical notation, we label the occupied orbitals with an index i and the unoccupied ones with an index a.

From time-dependent perturbation theory for a system of noninteracting electrons, one can calculate the linear response function,[40,41]

$$\chi^{(0)}(\mathbf{r}, \mathbf{r}', \omega) = -2e\sum_{ia} \phi_i^*(\mathbf{r})\phi_a(\mathbf{r})\phi_i(\mathbf{r}')\phi_a^*(\mathbf{r}') \times \frac{2(\varepsilon_a - \varepsilon_i)}{(\varepsilon_a - \varepsilon_i)^2 - \hbar^2\omega^2} \tag{14}$$

This response function contains no interaction effects of the electrons (except for the interaction effects that are included within the orbitals, e.g., within the Hartree or Kohn−Sham approximation) and can serve as an approximation for χ_{irr}. This approximation of using the response function of a noninteracting reference system for χ_{irr} is called Random-Phase Approximation (RPA). It is closely related to time-dependent density-functional theory (TDDFT),[42−45] where $\chi^{(0)}$ is also used for the irreducible response function, but where an exchange−correlation kernel f_{xc} enters in addition to the Coulomb kernel in eq 5. The poles of $\chi^{(0)}$ describe excitations from occupied to unoccupied states and correspond to orbital energy differences, i.e., $\omega = (\varepsilon_a - \varepsilon_i)/\hbar$.

2.4. Three-Dimensional Electron Gas.

We consider a noninteracting homogeneous electron gas with volume V. The single-particle states are given by plane waves,

$$\varphi_{\boldsymbol{k}}(\boldsymbol{r}) = \frac{1}{\sqrt{V}}\exp(\mathrm{i}\boldsymbol{k}\cdot\boldsymbol{r}) \tag{15}$$

which can be classified by their wavevector $\boldsymbol{k}$ due to the translational invariance. Consequently, the single-particle (orbital) energies become a function of the wavevector, the so-called dispersion,

$$\varepsilon(\mathbf{k}) = \frac{\hbar^2k^2}{2m} \tag{16}$$

where $k = |\mathbf{k}|$. The energy of the highest occupied state is the Fermi energy E_{F}, with the corresponding absolute value of the wavevector k_{F}.

The separation of the electronic excitations into single-particle excitations and plasmons introduced above is applicable here. Therefore, we treat single-particle excitations and plasmons separately by determining the poles of the irreducible response function χ_{irr}, approximated by $\chi^{(0)}$ within the RPA, and the zeros of the dielectric function ε, respectively. Subsequently, we clarify why this separate treatment is indeed appropriate and when it breaks down.

The possible single-particle excitation energies (i.e., the poles of $\chi^{(0)}$) are obtained by subtracting the energy of the state with wavevectors $\boldsymbol{k}$ below the Fermi energy from a state with wavevector $\boldsymbol{k} + \boldsymbol{q}$ above the Fermi level, where the wavevector of the single-particle excitation is $\boldsymbol{q}$. Thus, the single-particle excitation energy is

$$\Delta\varepsilon_{\text{sp}}(\mathbf{k}, \mathbf{q}) = \varepsilon(\mathbf{k} + \mathbf{q}) - \varepsilon(\mathbf{k}) = \frac{\hbar^2}{m}\mathbf{k}\cdot\mathbf{q} + \frac{\hbar^2}{2m}q^2 \tag{17}$$

In macroscopic systems (i.e., in the limit that the volume V goes to infinity), the wavevectors can be treated as continuous, and from the boundary conditions $|\boldsymbol{k}| \le k_{\text{F}}$ and $|\boldsymbol{k} + \boldsymbol{q}| \ge k_{\text{F}}$ one finds for the single-particle continuum $\Delta\varepsilon_{\text{sp}}$,[25]

$$\Delta\varepsilon_{\text{sp}}(q) \le \hbar v_{\text{F}}q + \frac{\hbar^2}{2m}q^2 \tag{18}$$

$$\Delta\varepsilon_{\text{sp}}(q) \ge -\hbar v_{\text{F}}q + \frac{\hbar^2}{2m}q^2, \text{ if } q > 2k_{\text{F}} \tag{19}$$

where we introduced the Fermi velocity $v_{\text{F}} = \hbar k_{\text{F}}/m$.

To determine the energies of the plasmonic excitations, we calculate the density response function within the RPA by taking the Fourier transform of eq 14,

$$\chi^{(0)}(\mathbf{q},\omega) = -\frac{2e}{(2\pi)^3}\int_{|\mathbf{k}|<k_F}\left(\frac{1}{\hbar\omega - \frac{\hbar^2}{2m}(\mathbf{k}^2 - [\mathbf{k}-\mathbf{q}]^2)} - \frac{1}{\hbar\omega - \frac{\hbar^2}{2m}([\mathbf{k}+\mathbf{q}]^2 - \mathbf{k}^2)}\right)\mathrm{d}^3k \qquad (20)$$

This integral can be evaluated analytically, and is given by the Lindhard function.[23] Here, it will be more convenient to perform a Taylor expansion for $qv_F \ll \omega$ up to forth order in $\mathbf{q}$, which leads to

$$\chi^{(0)}(\mathbf{q},\omega) = \frac{2e}{(2\pi)^3}\int_{|\mathbf{k}|<k_F}\left(\frac{q^2}{m\omega^2} + \frac{2\hbar(\mathbf{k}\cdot\mathbf{q})q^2}{m^2\omega^3} + \frac{3\hbar^2(\mathbf{k}\cdot\mathbf{q})^2q^2}{m^3\omega^4} + \cdots\right)\mathrm{d}^3k \qquad (21)$$

and the integration in spherical coordinates then yields

$$\chi^{(0)}(q,\omega) = \frac{e\rho_0 q^2}{m\omega^2}\left(1 + \frac{3}{5}\frac{v_F^2q^2}{\omega^2} + \cdots\right) \qquad (22)$$

where the electron density is given by $\rho_0 = k_F^3/3\pi^2$.

The dielectric function from eq 10 within the RPA has a very simple form after Fourier transformation,

$$\varepsilon(q,\omega) = 1 - \chi^{(0)}(q,\omega)f_{\mathrm{Coul}}(q) \qquad (23)$$

where the Fourier transform of the Coulomb kernel reads

$$f_{\mathrm{Coul}}(q) = \frac{4\pi e}{q^2} \qquad (24)$$

Finally, by calculating the zeros of the dielectric function, and performing a Taylor expansion of the appearing square root in $qv_F/\omega_{\mathrm{plas}}$, we can express the plasmon frequency as a function of the wavevector, which is the so-called plasmon dispersion,

$$\begin{aligned}\omega^2_{\mathrm{plas}}(q) &= \frac{e\rho_0}{m}q^2f_{\mathrm{Coul}}(q) + \frac{3}{5}\left(\frac{\hbar k_F}{m}q\right)^2\\ &= \frac{4\pi e^2\rho_0}{m} + \frac{3}{5}v_F^2q^2\end{aligned} \qquad (25)$$

The first term in eq 25 is exactly the same as the one found when calculating the plasmon frequency on purely classical grounds [cf. Section 2.1]. The second term can be interpreted as a "quantum kinetic-energy correction".

Both the single-particle continuum [eqs 18 and 19] and the plasmon dispersion [eq 25] are shown in Figure 1a for $\rho_0 = (1/6\pi^2)a_0^{-3}$, where $a_0 = \hbar^2/me^2$ is the Bohr radius. For small wavevectors, the plasmonic and single-particle excitations are well-separated. That is, at a given energy, plasmons and single-particle excitations have different wavevectors and because the wavevector characterizes the translational symmetry they cannot mix. Choosing a different value for ρ_0 will leave the single-particle continuum unchanged and only shift the plasmon dispersion. However, the qualitative picture will remain unchanged. Above a certain wavevector the plasmon dispersion penetrates the single-particle continuum. In this regime, the plasmonic excitations will mix single-particle excitations and the separate treatment breaks down if the mixing of plasmons and single-particle excitations is too strong. In this case, classifying the electronic excitations as plasmons and single-particle excitations is not possible anymore.

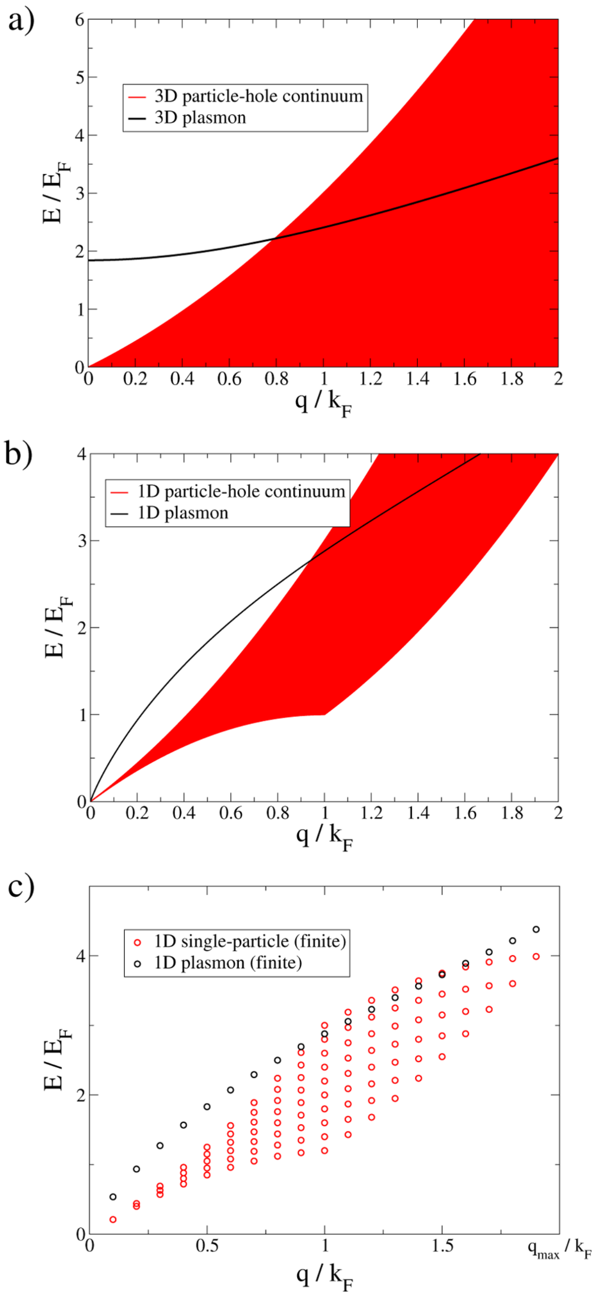

Figure 1. Plasmon dispersion and particle-hole continuum for (a) a three-dimensional electron gas with periodic boundary conditions for $\rho_0 = (1/8\pi^2)a_0^{-3}$, (b) a one-dimensional wire with periodic boundary conditions for $\rho_0 = (1/\pi)a_0^{-1}$ and $l = 20a_0$, and (c) a one-dimensional wire with finite size $L = 20\pi a_0$. The excitation vector is shown in units of the Fermi wave vector k_F, whereas the excitation energy is given in units of the Fermi energy E_F. See text for details.

2.5. One-Dimensional Electron Gas. For a one-dimensional (1D) homogeneous electron gas in a wire with length L, the single-particle states are plane waves,

$$\varphi_k(x) = \frac{1}{\sqrt{L}}\exp(ikx) \qquad (26)$$

and the dispersion is again given by

$$\varepsilon(k) = \frac{\hbar^2 k^2}{2m} \tag{27}$$

Again, we consider the limit of an infinite wire (i.e., $L \to \infty$) and treat the wavevector as continuous. The single-particle excitations can be determined in the same manner as for the 3D electron gas

$$\Delta\varepsilon_{\mathrm{sp}}(q) \leq \hbar v_{\mathrm{F}} q + \frac{\hbar^2 q^2}{2m} \tag{28}$$

$$\Delta\varepsilon_{\mathrm{sp}}(q) \geq \hbar v_{\mathrm{F}} q - \frac{\hbar^2 q^2}{2m}, \text{ if } q \leq k_{\mathrm{F}} \tag{29}$$

$$\Delta\varepsilon_{\mathrm{sp}}(q) \geq \frac{\hbar^2 q^2}{2m}, \text{ if } q \geq k_{\mathrm{F}} \tag{30}$$

Compared to the 3D electron gas considered in the previous section, the upper boundary is unchanged, but the lower boundary is modified.

For finding the plasmonic excitations, we again employ the RPA and start from $\chi^{(0)}$ [eq 14] and obtain after a 1D Fourier transformation,

$$\chi^{(0)}(q, \omega) = -\frac{2e}{2\pi} \int_{-k_{\mathrm{F}}}^{k_{\mathrm{F}}} \left(\frac{1}{\hbar\omega - \frac{\hbar^2}{2m}(k^2 - [k-q]^2)} - \frac{1}{\hbar\omega - \frac{\hbar^2}{2m}([k+q]^2 - k^2)} \right) \mathrm{d}k \tag{31}$$

As in the 3D case, we perform a Taylor expansion for $v_{\mathrm{F}} q \ll \omega$ up to fourth order in q and after integration arrive at,

$$\chi^{(0)}(q, \omega) = \frac{e\rho_0 q^2}{m\omega^2}\left(1 + \frac{v_{\mathrm{F}}^2 q^2}{\omega^2} + \cdots\right) \tag{32}$$

where $\rho_0 = 2k_{\mathrm{F}}/\pi$ is the one-dimensional electron density. The 1D Fourier transform of the 3D Coulomb kernel diverges, making it necessary to introduce a length parameter l modeling the width of the wire,[46]

$$f_{\mathrm{Coul}}(x) = \frac{e}{\sqrt{x^2 + l^2}} \tag{33}$$

The Fourier transform then reads

$$f_{\mathrm{Coul}}(q) = 2e\kappa_0(lq) \tag{34}$$

where κ_0 is the zeroth modified Bessel function of second kind.[47] Finally, the plasmon dispersion is determined by finding the zeros of the dielectric function ε [eq 23]. Again, a Taylor expansion in $v_{\mathrm{F}} q/\omega_{\mathrm{plas}}$ is used in order to simplify the appearing square root to arrive at

$$\omega_{\mathrm{plas}}^2(q) = \frac{2e^2\rho_0}{m}\kappa_0(lq)q^2 + v_{\mathrm{F}}^2 q^2 \tag{35}$$

Compared to the 3D electron gas, the first term, which arises from the classical restoring forces, now depends on the wavevector. This dependency reflects the fact that the electric field of a point charge drops with the square of the reciprocal distance, whereas in three dimensions the restoring force is independent of the distance.

In Figure 1b, the single-particle continuum and the plasmon dispersion in 1D are shown. For the plasmon dispersion, we chose $\rho_0 = (1/\pi)a_0^{-1}$ (which implies $k_{\mathrm{F}} = (1/2)a_0^{-1}$) and $l = 2a_0$. The plasmon dispersion now has a different behavior than in the 3D case, but for small wavevectors the plasmonic excitations are still well separated from the single-particle continuum. Thus, the separate treatment of plasmons and single-particle excitations is justified in this regime. This observation is independent of the specific choice of ρ_0 and l. However, for larger wavevectors the plasmon dispersion penetrates the single-particle continuum and the classification of excitations as plasmons or single-particle excitations will not be possible anymore if the mixing is strong.

2.6. Electron Gas in a Finite-Length Wire. In the previous subsections we have been concerned with the continuum limit, i.e., a continuous spectrum of single-particle energy levels. As a next step toward molecules, we now consider the situation where all wavevectors become quantized due to the boundary conditions that the electronic wave function has to vanish at the ends of the finite wire. We implement this by the selection rules

$$k_n = \frac{\pi}{L}n \text{ with } n = 1, 2, 3, \ldots \tag{36}$$

In addition, we assume that there is an upper bound for the wavevector, i.e., $k_n \leq k_{\mathrm{max}}$, which corresponds to a wire modeled by a discrete set of space points.

The single-particle wave functions that obey the boundary conditions are

$$\varphi_n(x) = \sqrt{\frac{2}{L}}\sin(k_n x) \tag{37}$$

and the single particle energies do not form a continuous spectrum anymore, but are discrete,

$$\varepsilon_n = \frac{\hbar^2 k_n^2}{2m} = \frac{\hbar^2\pi^2}{2mL^2}n^2 \tag{38}$$

For the possible single-particle excitations, the upper bound for the wavevector results in an additional boundary,

$$\Delta\varepsilon_{\mathrm{sp}}(q) \leq \frac{\hbar^2}{m}k_{\mathrm{max}}q - \frac{\hbar^2 q^2}{2m}, \text{ if } q > k_{\mathrm{max}} - k_{\mathrm{F}} \tag{39}$$

Moreover, the quantization of the single-particle energies leads to a discrete set of possible single-particle excitations replacing the continuum, where

$$q_n = \frac{\pi}{L}n \text{ with } n = 1, 2, 3, \ldots \tag{40}$$

This is shown in Figure 1c, where due to the selection rules the single-particle continuum in the infinite 1D wire is replaced by a discrete set of single-particle excitation energies. In this figure, we used $k_{\mathrm{F}} = 10(\pi/L) = (1/2)a_0^{-1}$ and $k_{\mathrm{max}} = 20(\pi/L)$, which corresponds to a model with 20 electrons and 20 atomic sites in a wire of length $L = 20\pi a_0$. This chosen value of L is such that the same k_{F} as for the infinite 1D wire is obtained.

For calculating the plasmon dispersion, one proceeds as above and calculates the Fourier transformation of the RPA irreducible response function $\chi^{(0)}$. However, for a finite-length wire the translational symmetry is broken and the Fourier transform is not diagonal in k-space anymore. We ignore the off-diagonal elements and employ the additional approximation of using the $\chi^{(0)}(q,\omega)$ of the infinite 1D electron gas model [eq 32] instead. This corresponds to neglecting the additional

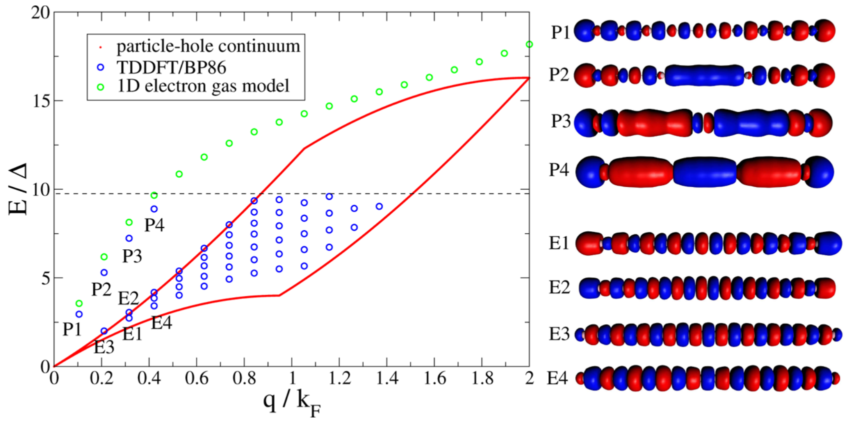

Figure 2. (a) Plasmon dispersion and particle-hole continuum of an Na_{20} chain calculated with (TD)DFT compared to the (finite) one-dimensional electron gas model. For TDDFT, only the 50 lowest excitations are calculated, which is indicated by the black dashed line. The excitation vector is shown in units of the Fermi wave vector k_F, whereas the excitation energy is given relative to the HOMO−LUMO gap Δ. See text for details. (b) Isosurface plots of the TDDFT transition densities of the four lowest plasmonic (P1−P4) and single-particle (E1−E4) excitations.

oscillations in the induced density occurring due to the boundary conditions.

Within this approximation, plasmons are affected by the boundary conditions only because of the quantization of excitation wavevector q according to eq 40. The resulting plasmonic excitations are included in Figure 1c. We observe that also for the finite length 1D wire the distinction of plasmons and single-particle resonances is meaningful for small wavevectors. Note, however, that because the translational invariance is lost, the wavevector does not distinguish excitations of different symmetry anymore and plasmons and single-particle excitations that are close in energy could exhibit some mixing even if their wavevector differs. Therefore, we will verify the model considered here by comparing to full molecular calculations in the following.

3. PLASMONS IN MOLECULES

We are now in the position to consider plasmons in molecular systems. As a first simple example, we use a sodium chain consisting of 20 atoms in a linear arrangement. Such linear sodium chains are a typical example of a molecular system in which the intense electronic excitations are commonly discussed as plasmons and for which classical models are often appropriate.[48] First, we performed a ground-state density-functional theory (DFT) calculation in order to determine the single-particle energies and orbitals. Subsequently, the electronic excitations were computed with TDDFT.

To analyze the resulting excitations in the same fashion as in the previous section, we have to classify the excitations by a wavevector q_n. To this end, we assigned a wave vector $k_n = (\pi/L)n$ to each molecular orbital by visual inspection, i.e., by setting n to the number of nodes of the ground-state orbitals. Armed with this knowledge, we can assign a wavevector to each orbital transition by subtracting the wavevectors of the involved orbitals. The electronic excitations as described within TDDFT are superpositions of orbital transitions and, therefore, can be assigned a wavevector $q_n = (\pi/L)n$ by using the dominant contribution of orbital transitions. For the linear sodium chain, such an assignment is possible because each excitation is either dominated by a single orbital transition or the different contributing orbital transitions correspond to the same wavevector.

In Figure 2, the excitation energies (blue circles) are plotted against the assigned wavevector divided by the Fermi wavevector, $k_n/k_F = n/10$, to obtain a plot similar to those discussed in the previous section. For each wavevector, we observe that one excitation is well separated from the others. Thus, by analogy with the results obtained earlier for the electron gas models, these excitations can be identified as plasmons, while the remaining excitations correspond to single-particle excitations.

To make the analogy more obvious, we employ the electron gas model for the 1D wire presented in the previous section in order to calculate the boundaries of the single-particle excitation continuum and the plasmonic excitation energies. For this purpose, we determined v_F (or equivalently L) by fitting the Kohn−Sham dispersion relation extracted from the ground-state DFT calculations to eq 38. With this value, the boundaries of the single-particle continuum of the 1D electron gas with an upper bound for the wavevector [eqs 28−30 and 39] are calculated and included in Figure 2 (red line). We find that the excitations obtained with TDDFT and identified as single-particle excitations fall nicely within the boundaries of the single-particle continuum obtained for the 1D electron gas.

In addition, the plasmonic excitation energies obtained for the finite 1D wire (cf. Section 2.6) are also shown in Figure 2 (green circles). One observes that the TDDFT excitations identified as plasmons are very close in energy to the values of the electron gas model. The deviations can be attributed to the limitations of this simple model and the *ad hoc* determination of the Fermi velocity v_F (or of the length L). This confirms the classification of the excitations obtained from TDDFT as either single-particle or plasmons. Note that this classification is still possible, even though the wavevector assigned here is only an approximate symmetry classification. In addition, the good agreement with the full TDDFT results also shows the validity of the electron gas model for the considered sodium chain.

Finally, we inspect the transition densities of the four lowest-energy plasmonic and single-particle excitations. These are shown in Figure 2 as isosurface plots. The transition densities of the plasmons have an envelope with a number of nodes increasing from one to four, i.e., equal to n in the assigned wavevector $q_n = (\pi/L)n$. This is in line with the classical interpretation of plasmons as collective electronic excitations that have the form of standing density waves. The additional

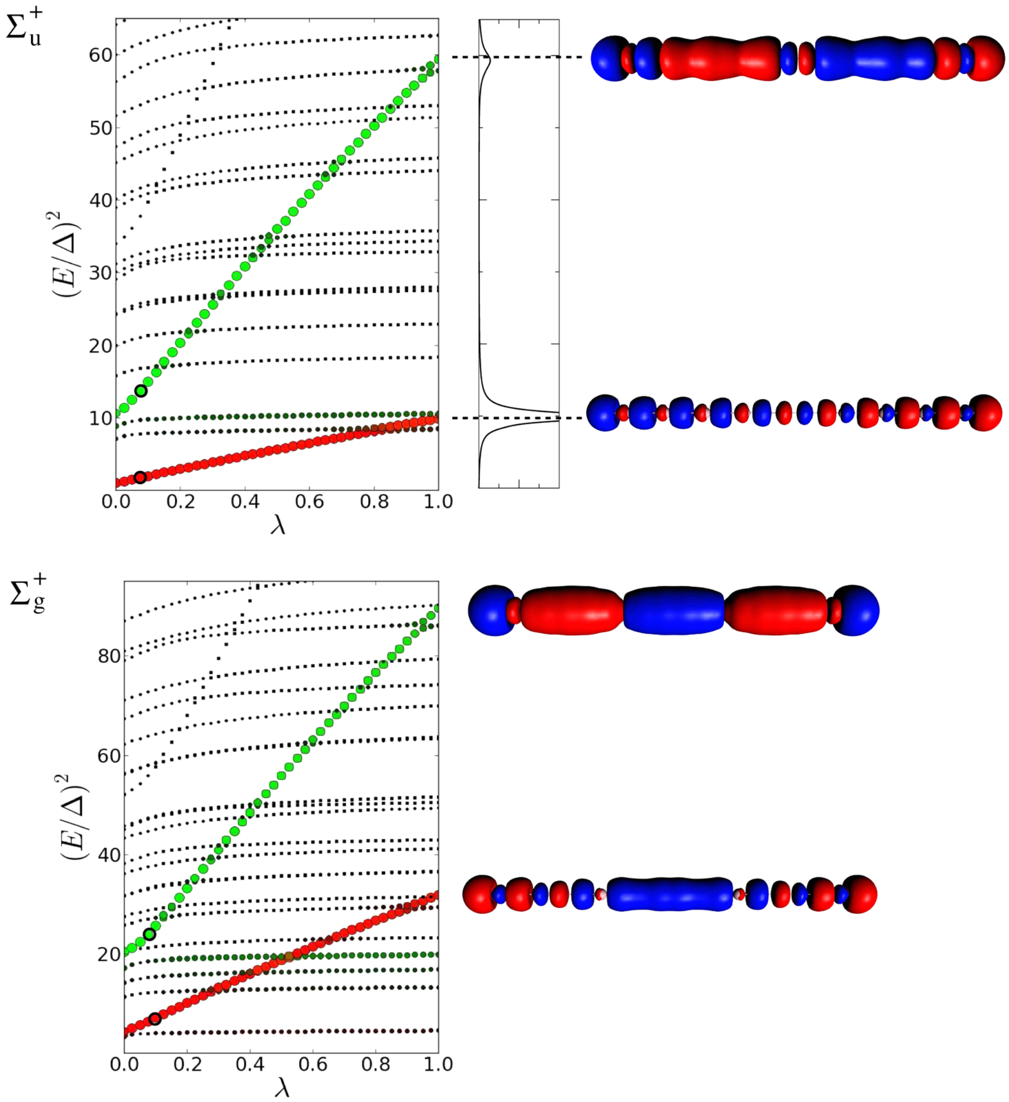

Figure 3. Change of the squared excitation energies of a sodium chain consisting of 20 atoms upon scaling the electronic interaction (left) and isosurface plots of the identified plasmons (right). Excitation energies are plotted in units of the HOMO−LUMO gap (Δ = 0.17 eV) and the coloring scheme described in the text is used to follow the plasmonic excitations, using the excitations highlighted by a black circle at λ = 0.1 as reference points. For dipole-allowed excitations, the linear absorption spectrum is also included.

oscillations observed in the transition densities result from the finite size. On the other hand, the transition densities of the single-particle excitations show no envelope with a low wavevector. Looking, e.g., at the third single-particle excitation (labeled E3 in the figure), it is not immediately obvious why this excitation is classified by the same wavevector as the second plasmon (labeled P2 in the figure). Here, the dominant contributions of the orbital transitions can also be classified by the same wavevector. However, the mixing of the contributing orbital transitions leads to destructive interference for the long-wavelength components and results in a transition density where the wavevector is not apparent anymore.

4. IDENTIFYING PLASMONIC EXCITATIONS

4.1. Scaling Approach for Time-Dependent DFT. So far, the identification of plasmons has been based on the assignment of wavevectors to the individual excitations. For general molecules, however, such an assignment is not possible anymore. Because there is no translational symmetry, neither the electronic states nor the electronic excitations can be classified by a wavevector. Consequently, pictures such as in Figure 2 can only be obtained for special cases such as simple linear chains. One might wonder whether inspecting the transition densities could allow for the distinction of plasmons and single-particle excitations, but this becomes cumbersome and requires prior knowledge of the expected plasmonic transition densities. Alternatively, one might expect that the oscillator strengths could provide a possibility for identifying plasmonic resonances. However, this is also not a reliable procedure. For instance, the electric dipole oscillator strengths of the plasmons of a linear chain with an even number of nodes vanish, even though these have a large induced density.

For developing a simple way of identifying plasmonic excitations, we recall that in Section 2.2 we noticed that poles of the irreducible response function (i.e., single-particle excitations) and zero modes of the dielectric function (i.e., plasmons) exhibit a different dependence on the electron−electron interaction contained in f_{Coul} when it is gradually “switched on”. In order to monitor the dependence of the excitation energies on f_{Coul}, we decided to scale the electron−

electron interaction term in the response equations. As an example we will discuss such a scaling approach for TDDFT.

Within the framework of TDDFT, the interacting system is mapped onto a noninteracting (Kohn−Sham) reference system.[43,45] This results in an integral equation for the external response function that closely resembles eq 9

$$\int \varepsilon^{\mathrm{TDDFT}}(\mathbf{r}, \mathbf{r}'', \omega)\chi_{\mathrm{ext}}(\mathbf{r}'', \mathbf{r}', \omega)\, \mathrm{d}^3r'' = \chi^{(0)}(\mathbf{r}, \mathbf{r}', \omega) \tag{41}$$

where $\chi^{(0)}$ is the density response function of the noninteracting Kohn−Sham reference system introduced earlier and the dielectric function,

$$\begin{aligned}\varepsilon^{\mathrm{TDDFT}}(\mathbf{r}, \mathbf{r}'', \omega) = {}& \delta(\mathbf{r} - \mathbf{r}'') \\ & - \int \chi^{(0)}(\mathbf{r}, \mathbf{r}''', \omega)[f_{\mathrm{Coul}}(\mathbf{r}''' - \mathbf{r}'') \\ & + f_{\mathrm{xc}}(\mathbf{r}''', \mathbf{r}'', \omega)]\, \mathrm{d}^3r'''\end{aligned} \tag{42}$$

now contains the frequency-dependent exchange−correlation kernel $f_{\mathrm{xc}}(r,r',\omega)$ in addition to the Coulomb kernel. The density response function of the Kohn−Sham system is given by eq 14 where the Kohn−Sham orbitals and their orbital energies are used, i.e., it is equivalent to the RPA response function. The excitation energies of the Kohn−Sham reference system are given by orbital-energy differences, whereas the true excitation energies are obtained by analyzing the poles of χ_{ext}.

To make a smooth transition between the noninteracting and the interacting system, we introduce a dimensionless scaling factor λ taking values between zero and one in eq 42,

$$\begin{aligned}\varepsilon^{\mathrm{TDDFT}}(\mathbf{r}, \mathbf{r}'', \omega) = {}& \delta(\mathbf{r} - \mathbf{r}'') \\ & - \lambda \int \chi^{(0)}(\mathbf{r}, \mathbf{r}''', \omega)[f_{\mathrm{Coul}}(\mathbf{r}''' - \mathbf{r}'') \\ & + f_{\mathrm{xc}}(\mathbf{r}''', \mathbf{r}'', \omega)]\, \mathrm{d}^3r'''\end{aligned} \tag{43}$$

The excitation energies then become a function of the scaling parameter λ. Here, we have chosen to scale both the Coulomb kernel and the exchange−correlation kernel simultaneously, because both emerge from the electron−electron interaction.

In practical TDDFT calculations one employs the adiabatic approximation and neglects the frequency dependence of the exchange−correlation kernel. The induced density is typically expanded in the products of occupied and virtual Kohn−Sham molecular orbitals,

$$\delta\rho(\mathbf{r}) = \sum_{i,a} X_{ia}\phi_i(\mathbf{r})\phi_a^*(\mathbf{r}) + Y_{ia}\phi_i^*(\mathbf{r})\phi_a(\mathbf{r}) \tag{44}$$

and eq 41 leads to the TDDFT eigenvalue equations[42,44]

$$\begin{pmatrix} \boldsymbol{A} & \boldsymbol{B} \\ -\boldsymbol{B} & -\boldsymbol{A} \end{pmatrix}\begin{pmatrix} \boldsymbol{X} \\ \boldsymbol{Y} \end{pmatrix} = \hbar\omega \begin{pmatrix} \boldsymbol{X} \\ \boldsymbol{Y} \end{pmatrix} \tag{45}$$

where the matrices $\boldsymbol{A}$ and $\boldsymbol{B}$ are given by

$$A_{ia,jb} = (\varepsilon_a - \varepsilon_i)\delta_{ij}\delta_{ab} + \lambda[2(ia|jb) + 2f_{iajb}^{\mathrm{xc}}] \tag{46}$$

$$B_{ia,jb} = \lambda[2(ia|jb) + 2f_{iajb}^{\mathrm{xc}}] \tag{47}$$

with the matrix elements of the Coulomb and exchange−correlation kernels, respectively,

$$(ia|jb) = e\iint \phi_i(\mathbf{r})\phi_a(\mathbf{r})f_{\mathrm{Coul}}(\mathbf{r} - \mathbf{r}')\phi_j(\mathbf{r}')\phi_b(\mathbf{r}')\, \mathrm{d}^3r\, \mathrm{d}^3r' \tag{48}$$

$$f_{iajb}^{\mathrm{xc}}(\omega) = e\iint \phi_i(\mathbf{r})\phi_a(\mathbf{r})f_{\mathrm{xc}}(\mathbf{r}, \mathbf{r}')\phi_j(\mathbf{r}')\phi_b(\mathbf{r}')\, \mathrm{d}^3r\, \mathrm{d}^3r' \tag{49}$$

Thus, compared to a standard TDDFT calculation, the matrix elements of the Coulomb and exchange−correlation kernels are multiplied by the scaling parameter λ. Note that scaling the electron−electron interaction does not require the calculation of new integrals, making it trivial to implement in quantum chemistry codes.

4.2. Scaling Approach Applied to Na_{20} Chain. To test the scaling approach for identifying plasmons, we revisit the sodium chain consisting of 20 atoms considered earlier in Section 3. We calculated the electronic excitation energies using TDDFT with increasing values of λ and depicted the results in Figure 3, where the symmetries Σ_u^+ and Σ_g^+ are considered separately.

By studying the change of the calculated excitation energies as a function of the scaling parameter λ one can clearly distinguish different types of excitations: Most excitation energies only change slightly when increasing the scaling parameter λ, i.e., they are close to an orbital energy difference of the Kohn−Sham reference system for all values of λ. These excitations can be classified as single-particle excitations and are exactly those excitations that lie within the single-particle continuum as depicted in Figure 2.

For a few excitations, the excitation energy shows a strong dependence on the scaling parameter λ. These excitations will be denoted as plasmonic excitations, as the transition from the reference system to the fully interacting system is mainly determined by the electric restoring forces encoded in f_{Coul}. For $\lambda = 0$ these modes lie in the single-particle continuum of Figure 2, but they move outside upon increasing λ and coincide with the plasmonic resonances in Figure 2 for $\lambda = 1$. These plasmonic excitations are identical with those identified already in Section 3 and their transition densities have the form of standing waves with an increasing number of nodes. For the excitations with Σ_u^+ symmetry the absorption spectrum is also included in Figure 3. Here, we find that the identified plasmons with one and with three nodes correspond to the only excitations that have a significant oscillator strength.

To identify the expected behavior of plasmonic excitations, we revisit the 1D electron gas and introduce a scaling of the Coulomb kernel by replacing $f_{\mathrm{Coul}}(q)$ by $\lambda f_{\mathrm{Coul}}(q)$. The 1D plasmons in this model are then given by [cf. eq 35]

$$\omega_{\mathrm{plas}}^2(q) = \frac{e\rho_0}{m}\lambda f_{\mathrm{Coul}}(q)q^2 + v_{\mathrm{F}}^2q^2 \tag{50}$$

that is, the squared plasmonic excitation energies $\hbar^2\omega_{\mathrm{plas}}{}^2$ increase linearly with λ. The same dependence on the Coulomb kernel is also found for the 3D electron gas [cf. eq 25]. Therefore, we have plotted the squared excitation energies in Figure 3. In addition, we have divided the squared excitation energies by the squared energy difference between the highest occupied and the lowest unoccupied molecular orbitals (HOMO−LUMO gap) Δ, i.e., plot $\hbar^2\omega^2/\Delta^2$ as a function of λ. For $\lambda = 0$, the first term disappears and for systems with a similar electronic structure the second term will then only depend on the number of nodes of the plasmon, i.e., the plasmonic excitation energies should start at the same point for $\lambda = 0$.

To follow the plasmonic excitations when increasing the scaling parameter λ, we have employed a coloring scheme in our plots: First, we select candidates for plasmonic excitations

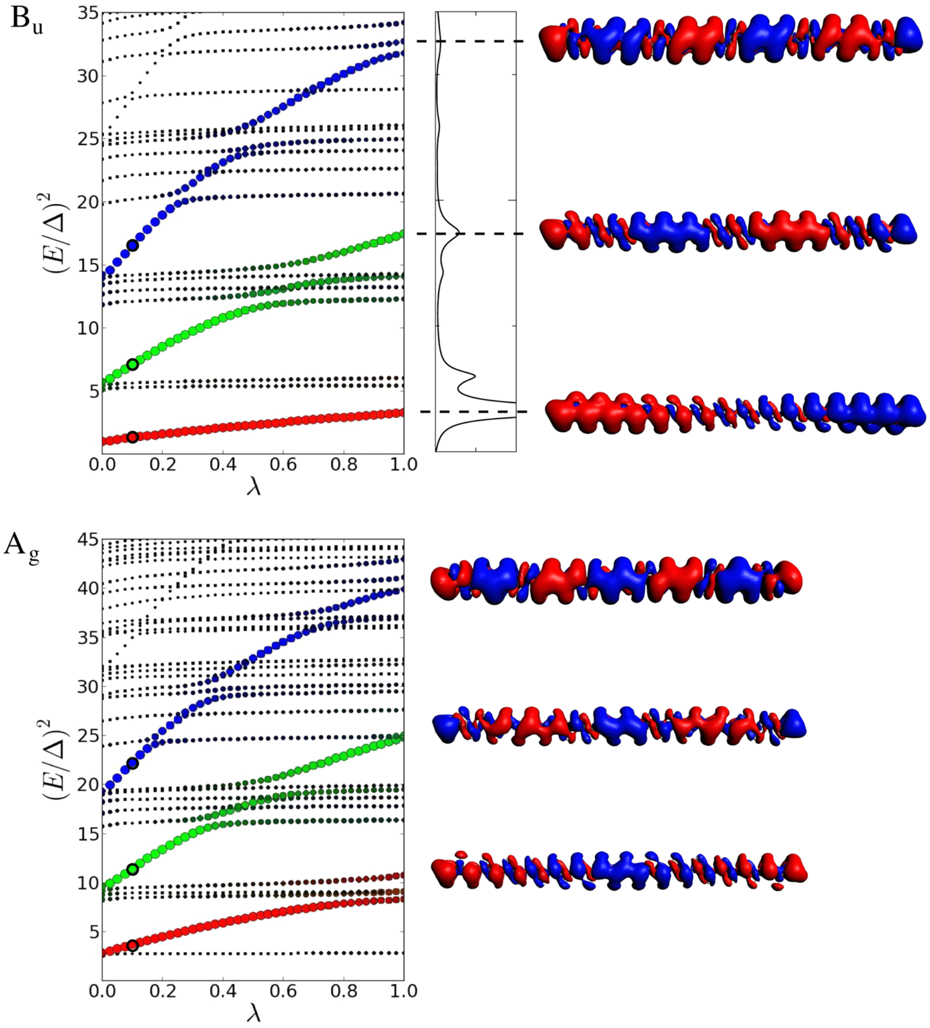

Figure 4. Change of the squared excitation energies of $C_{30}H_{32}$ alkene chain upon scaling the electronic interaction (left) and isosurface plots of the identified plasmons (right). Excitation energies are plotted in units of the HOMO−LUMO gap ($\Delta = 0.84$ eV) and the coloring scheme described in the text is used to follow the plasmonic excitations, using the excitations highlighted by a black circle at $\lambda = 0.1$ as reference points. For dipole-allowed excitations, the linear absorption spectrum is also included.

by visual inspection for a certain value of λ at which a linear increase is clearly visible. In Figure 3, we chose $\lambda = 0.1$ as reference point. For these reference excitations, their similarity to all other excitations at different values of λ is determined by calculating the scalar product of the corresponding eigenvectors of the TDDFT eigenvalue problem.[49] All points in the plot are then colored by using the additive RGB color model where the amount of added color red, green, and blue is given by the scalar product with the first, second, and third reference excitation, respectively. In addition, the size of the points is increased with the absolute value of the sum of these scalar products. For the sodium chain considered here, we observe that the composition of the TDDFT eigenvectors of the plasmonic excitations is identical for all values of λ. Furthermore, one notices that the plasmonic excitations do not mix with single-particle excitations even if these come close in energy. Thus, for the sodium chain the wavevector assigned in Section 3 still serves as an (approximate) symmetry classification that prevents this mixing.

Finally, we note that a third type of excitations could possibly also be identified in the plots of the excitation energies as a function of the scaling parameter λ: If the excitation energy decreases when increasing λ, the Coulomb attraction of the electron and the hole, which should be accounted for by the exchange−correlation kernel f_{xc}, is the decisive contribution to the excitation energy. Such excitations are usually classified as charge-transfer excitations or excitons. However, as these excitations are not treated properly by TDDFT with standard nonhybrid functionals,[50,51] these cannot be found here and will, therefore, not be discussed further.

5. IDENTIFYING PLASMONS IN MOLECULAR CHAINS

5.1. $C_{30}H_{32}$ Chain. As a slightly more complicated example, we consider an *all-trans*-alkene chain with 30 carbon atoms. This alkene chain is an organic molecule with a HOMO−LUMO gap that is significantly larger than in the sodium chain (i.e., 0.84 eV compared to 0.17 eV). Moreover, it is not linear, but has C_{2h} symmetry. First, we calculated the ground-state Kohn−Sham orbitals and orbital energies of the π-system and verified by visual inspection that each π-orbital could still be assigned a wavevector. This suggests that one should be able to clearly distinguish plasmonic excitations with specific wavevectors from the single-particle excitations.

Subsequently, we determined the excitation energies via TDDFT calculations and changed the values of the scaling

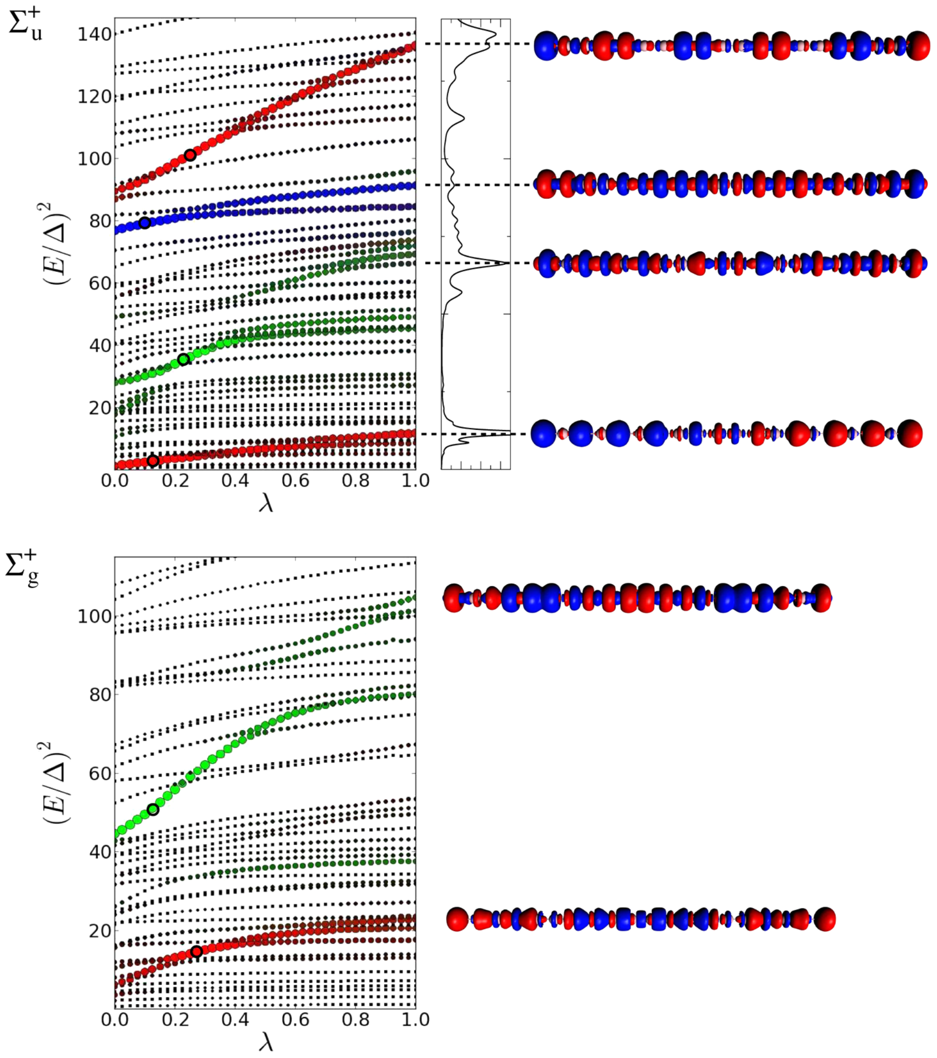

Figure 5. Change of the squared excitation energies of a gold chain consisting of 20 atoms upon scaling the electronic interaction (left) and isosurface plots of the identified plasmons (right). Excitation energies are plotted in units of the HOMO−LUMO gap (Δ = 0.18 eV) and the coloring scheme described in the text is used to follow the plasmonic excitations, using the excitations highlighted by a black circle as reference points. For dipole-allowed excitations, the linear absorption spectrum is also included.

parameter from $\lambda = 0$ to $\lambda = 1$. As before, the dependence of the squared excitation energies is shown in Figure 4 for excitations with B_u and A_g symmetry. As for the sodium chain, we can clearly distinguish single-particle excitations, for which the excitation energy is largely independent of the scaling parameter, and plasmons, for which the squared excitation energy increases linearly with λ.

However, in contrast to the sodium chain we now observe "avoided crossings" if these plasmons come close to single-particle excitations. In this case, plasmons and single-particle excitations mix, since they no longer belong to different symmetries. In some cases, such as the lowest-energy plasmon in symmetry A_g, this mixing of plasmons and single-particle excitations also occurs for $\lambda = 1$, i.e., the distinction partly breaks down. Nevertheless, the corresponding transition densities, which are also shown in Figure 4, still show a standing wave pattern with an envelope that has an increasing number of nodes for those excitations that have the largest plasmonic contribution according to our coloring scheme (i.e., those with the largest similarity with the reference plasmonic excitation identified at $\lambda = 0.1$).

For the excitations with B_u symmetry, the linear absorption spectrum also included in Figure 4 again shows that the identified plasmonic excitations are the ones with the largest oscillator strengths. However, there are also single-particle excitations with a significant intensity, such as the second and third excitation. In addition, some single-particle excitations gain oscillator strength due to mixing with plasmons, such as the excitation below the second plasmon in this symmetry.

5.2. Au_{20} Chain. As a more complicated example of a molecular chain, we consider a chain of 20 gold atoms. Compared to the sodium chain, the electronic structure now becomes more complicated because in addition to the s-orbitals, the occupied Au d-orbitals are now also in the relevant energy range.[48,52]

Plots of the squared excitation energies as functions of the scaling of the electron−electron interaction are shown in Figure 5 separately for the Σ_u^+ and Σ_g^+ symmetries. These plots appear more complicated than for the sodium chain, but it is nevertheless still possible to identify plasmonic excitations for which the squared excitation energy increases strongly with λ. The lowest-energy plasmon has Σ_u^+ symmetry and shows a behavior that is similar to the one found for the lowest-energy plasmon in the sodium chain. Because there are more single-particle excitations at low energies, avoided crossings appear, but overall the composition of this first plasmonic excitation is preserved when going from $\lambda = 0$ to $\lambda = 1$. This lowest-energy plasmon has a large dipole oscillator strength and can be identified with the first strong peak in the calculated optical spectrum of a Au_{20} chain at ca. 0.6 eV,[36,52] which can also be seen in the linear absorption spectrum included in Figure 5. Its transition density, which is also included in Figure 5, has one node and is similar to the one of the first plasmon in the Na_{20} chain. Thus, the lowest-energy plasmon in the Au_{20} chain can be assigned to a transition from occupied to unoccupied s-orbitals, even though mixing of the occupied s-orbitals with d-orbitals leads to deviations from the pure s-orbital transitions observed for the sodium chain.

Finding the second plasmon in the Σ_u^+ symmetry is more difficult. For $\lambda = 0.25$ it is possible to identify one excitation for which a linear increase of the square excitation energy with λ is apparent. Following this excitation by calculating the overlap of the reference excitation with the other excitations at higher values of λ shows that this plasmon strongly mixes with single-particle excitations. For $\lambda = 1$, the plasmonic excitation contributes to a number of different excitations. All these excitations gain dipole oscillator strength by this mechanism, which results in a broad band with distinct peaks in the region between ca. 1.2 eV and ca. 1.7 eV of the calculated optical spectrum.[52] For the excitation with the largest plasmonic contribution, the transition density is included in the figure and shows contributions from both s- and d-orbitals. A third plasmon is found at slightly higher energies, which also mixes with single-particle excitations. The transition densities of both the second and the third identified plasmon with Σ_u^+ symmetry can be characterized by an envelope with three nodes.

This strong mixing can be understood by realizing that for gold chains, both intraband transitions between occupied and unoccupied s-orbitals and interband transitions between occupied d-orbitals and unoccupied s-orbitals are possible. The plasmons are due to s−s intraband transitions. For the lowest wavevector, i.e., the first plasmon with only one node, the s−d interband single-particle excitations with the same wavevector are higher in energy. However, for the plasmon with three nodes, the plasmonic s−s excitations move inside the energy range of the s−d interband single-particle excitations with the same wavevector as λ is increased. Since the plasmon and the single-particle excitations have the same wavevector, they mix and the resulting excitations have contributions both from the intraband plasmonic excitations and from interband single-particle excitations. Hence, the clear distinction of plasmons and single-particle excitations breaks down here.

At even higher energies, an additional plasmon with Σ_u^+ symmetry with five nodes is found. Here, we observe a clear linear increase of the squared excitation energy with λ. Moreover, this plasmonic excitation does not mix with any other excitations and its composition is identical for different values of λ. Thus, the plasmonic excitation energy is not close to interband single-particle excitation with the same wavevector anymore. Finally, for the Σ_g^+ symmetry, we can identify plasmons with two and four nodes, respectively. In both cases, these plasmons mix with single-particle excitations. For the plasmon with two nodes, this is apparent from the decreased slope found for larger values of λ, whereas for the plasmon with four nodes the plasmonic excitation strongly mixes with different single-particle excitations for $\lambda > 0.6$.

6. IDENTIFYING PLASMONS IN MOLECULAR CLUSTERS

6.1. Na_{20} Cluster.

After discussing the identification of plasmons in molecular chains, we now turn to small molecular clusters. First, we consider a tetrahedral Na_{20} cluster. Compared to the previously discussed sodium chains, the electronic excitations cannot be easily classified by a wavevector anymore. Instead, one has to use the irreducible representations of the point group T_d to distinguish excitations of different symmetries.

The dependence of the squared excitation energies on the scaling parameter λ for the electron−electron interaction is shown in Figure 6. We performed the response calculations for all possible symmetries of the excitation, but show only the results for the symmetries A_1, E, and T_2 where low-lying plasmons could be identified. Again, we employed the coloring scheme introduced above to follow the plasmonic excitations in these plots, using a point at which the linear increase of the plasmonic excitation energy is obvious as reference. These reference points are highlighted with a black circle in the plots.

The lowest-energy plasmon is found in the T_2-symmetry and can be identified easily in the plots, as it corresponds to the only excitation for which a linear increase of the squared excitation energy with λ is observed. For some values of λ, the energy of this plasmonic excitation is close to single-particle excitations and avoided crossings appear. Nevertheless, the composition of the plasmonic excitation only changes slightly when increasing λ, and a single excitation can be identified as plasmon at $\lambda = 1$. The corresponding transition density is included in Figure 6 and shows that the plasmon corresponds to a density oscillation occurring along the tetrahedral S_4-axes with one nodal plane. This excitation corresponds to the intense plasmon peak in the linear absorption spectrum. Note that, as all excitations with T_2-symmetry, this lowest plasmon is 3-fold degenerate.

In a similar fashion, plasmons can be identified for the A_1 and E symmetries. The plasmonic excitation appearing in the totally symmetric A_1 irreducible representation looks like a “breathing mode”, in which the induced charge density at the corners of the tetrahedron has the opposite sign than at the core. Here, the mixing with single-particle excitations does not only cause avoided crossings, but also results in a deviation from the linear increase. Finally, we could identify two (doubly degenerate) plasmons with E-symmetry, for which the transition densities each exhibit two nodal planes. Note that even though there is a large induced density, the dipole oscillator strengths of the plasmons with A_1 and E symmetry vanish.

6.2. Ag_{20} Cluster.

As a second example of a metal cluster, we studied the electronic excitations in a tetrahedral Ag_{20} cluster. This cluster is often studied as a model for silver nanoclusters, for instance for investigating surface-enhanced Raman spectroscopy of molecules on metal clusters.[53] The plasmonic resonances of this and other silver clusters have been analyzed previously by using TDDFT.[32,33,54,55] For $\lambda = 1$, our results are identical with those presented in ref 32 for the same computational methodology.

Plots of the squared excitation energies as a function of the scaling parameter λ are shown in Figure 7 for the T_2, A_1, and E symmetries. Overall, the results are qualitatively similar to those obtained for the Na_{20} cluster. The lowest-energy plasmon is found in the T_2 symmetry and its transition density corresponds to a displacement of the density along the S_4

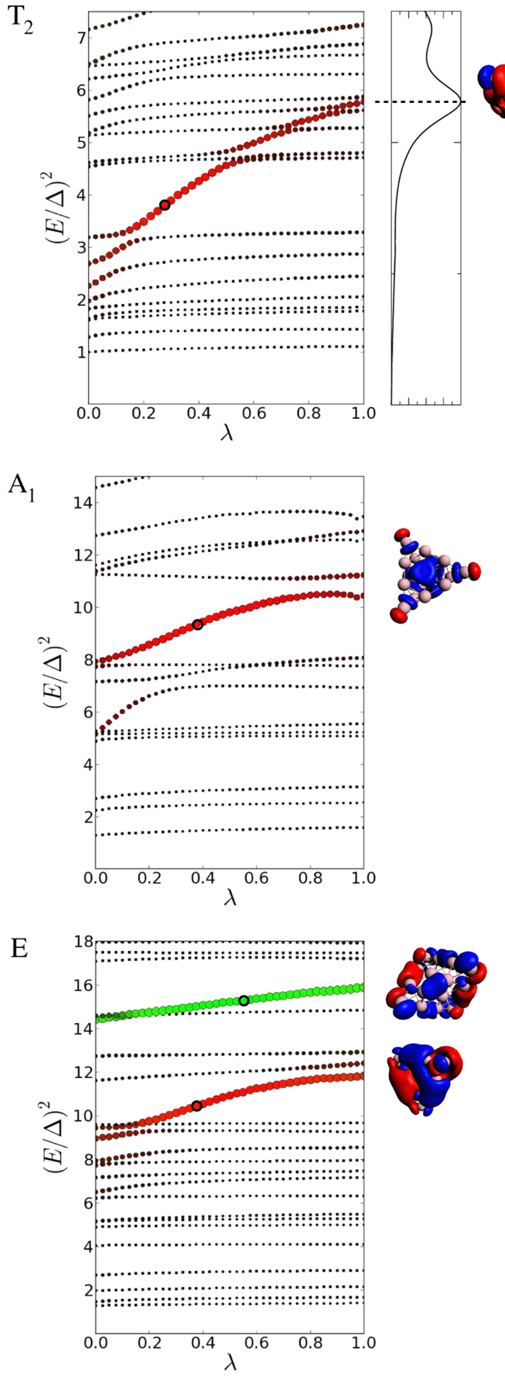

Figure 6. Change of the squared excitation energies of a tetrahedral Na_{20} cluster upon scaling the electronic interaction (left) and isosurface plots of the identified plasmons (right). Excitation energies are plotted in units of the HOMO−LUMO gap (Δ = 0.92 eV) and the coloring scheme described in the text is used to follow the plasmonic excitations, using the excitations highlighted by a black circle as reference points. For dipole-allowed excitations, the linear absorption spectrum is also included.

symmetry axis. The identified plasmonic excitation is mainly responsible for the strong peak in the optical spectrum of Ag_{20} calculated at 3.3 eV with BP86/TZP[32] (see also the linear absorption spectrum included in the figure). However, the coloring according to the overlap with the reference excitation at λ = 0.1 shows that the plasmonic excitation also mixes with two single-particle excitations at lower energies. Therefore, these single-particle excitations also gain dipole oscillation strengths and also contribute to the strong peak in the optical spectrum.

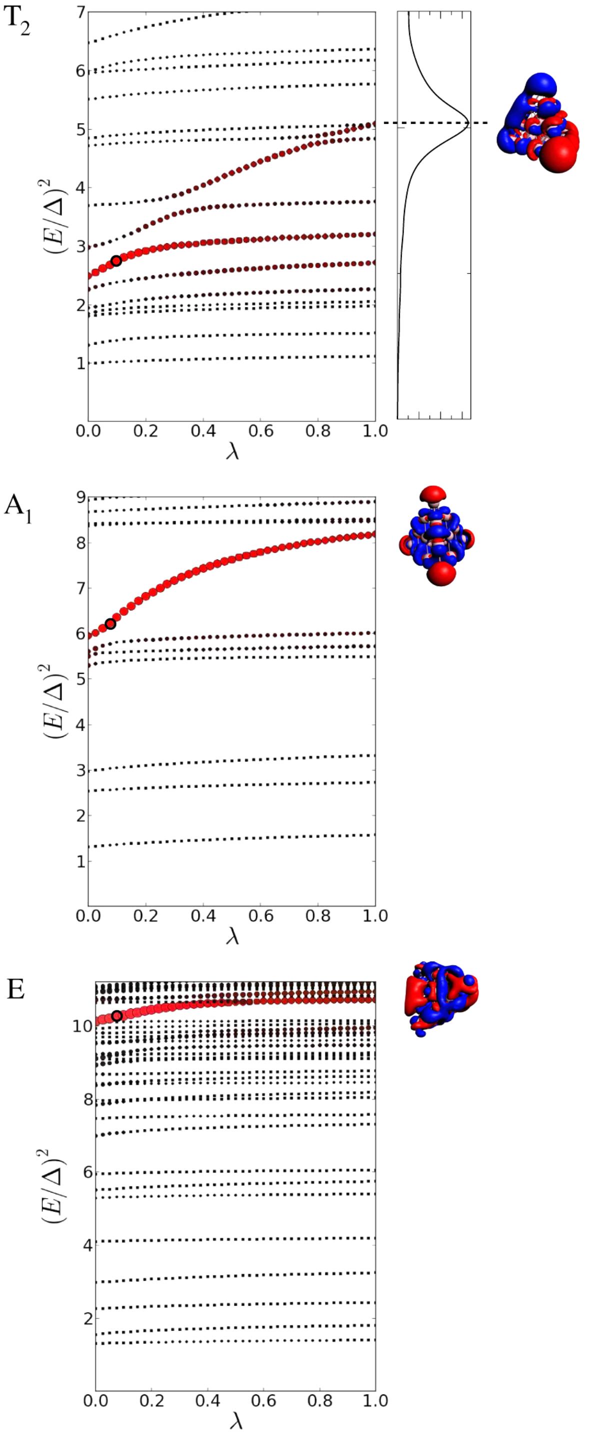

Figure 7. Change of the squared excitation energies of a tetrahedral Ag_{20} cluster upon scaling the electronic interaction (left) and isosurface plots of the identified plasmons (right). Excitation energies are plotted in units of the HOMO−LUMO gap (Δ = 1.49 eV) and the coloring scheme described in the text is used to follow the plasmonic excitations, using the excitations highlighted by a black circle as reference points. For dipole-allowed excitations, the linear absorption spectrum is also included.

Additional plasmons can also be identified for the A_1 and E symmetries. These show induced densities similar to those already identified in Na_{20} that correspond to a breathing mode and to a displacement of the density along the C_3 axis with two nodal planes. Even though these plasmons have a large induced density, their dipole oscillator strengths vanish because of their symmetry, and the lowest nonzero contributions to the oscillator strengths are due to the induced octupole and quadrupole moments, respectively.

6.3. Fullerene C_{60}.

Finally, we investigate C_{60} as an example of a molecule-like cluster. The first analysis of the plasmons of C_{60} was performed in ref 56. These calculations predicted strong peaks in the optical spectrum at ca. 6 eV and at ca. 20 eV, which were assigned to "π-plasmons" and "σ-plasmons", respectively. However, this early study did not distinguish plasmons and single-particle excitations. Subsequently, plasmons in fullerenes were investigated theoretically in more detail by Ju et al. using model calculations assuming a spherically symmetric system.[57] In this case, the plasmonic excitations may be labeled according to their angular momentum by quantum numbers (J,m_J). Only the plasmons corresponding to $J = 1$ have large dipole oscillator strengths and can be assigned to strong peaks in the optical spectrum of fullerenes.

The point group of C_{60} is I_h and the excitations with $J = 1$ in a spherically symmetric model belong to the irreducible representation T_{1u}, whereas those with $J = 2$ belong to the H_g representation. As icosahedral symmetry is not supported in our quantum-chemical calculations, all calculations have been performed for the D_{5d} point group. The previously discussed excitations then do not transform like single irreducible representations anymore, but the three degenerate excitations corresponding to $J = 1$ belong to A_{2u} and E_{1u}, whereas the five degenerate excitations corresponding to $J = 2$ belong to A_{1g}, E_{1g}, and E_{2g}. For simplicity, only the excitations transforming like the one-dimensional irreducible representations A_{2u} and A_{1g} are analyzed in the following.

The dependence of the squared excitation energies as calculated with TDDFT on the scaling parameter λ is depicted in Figure 8. For the excitations with A_{2u} symmetry, two plasmons with one nodal plane can be identified. These correspond to $J = 1$ and can be identified with the excitations assigned previously to the intense peaks at 5.9 eV and at 6.4 eV in the optical spectrum[58] (see also the linear absorption spectrum included in the figure). Even though these plasmonic excitations, in particular the second one, are close to single-particle excitations, virtually no mixing is observed here. In addition, a plasmon with three nodal planes (i.e., corresponding to $J = 3$) can be identified at higher excitation energy. Note, however, that also two of the lower-lying single-particle excitations have significant oscillator strengths and transition densities similar to those of the identified plasmons with $J = 1$. However, as their excitations energies do not increase with λ above ca. 0.5, we did not classify these excitations as plasmons.

For the excitations with A_{1g} symmetry, three plasmonic excitations can be found. These each have two nodal planes and correspond to $J = 2$. The lowest-energy plasmon starts to mix with single-particle excitations for higher values of λ, as can be seen from the change in the slope. Finally, we note that all plasmons identified here are due to transitions between π orbitals and can, therefore, be labeled π-plasmons, whereas transitions between σ-orbitals appear at excitation energies that are higher than those considered here.

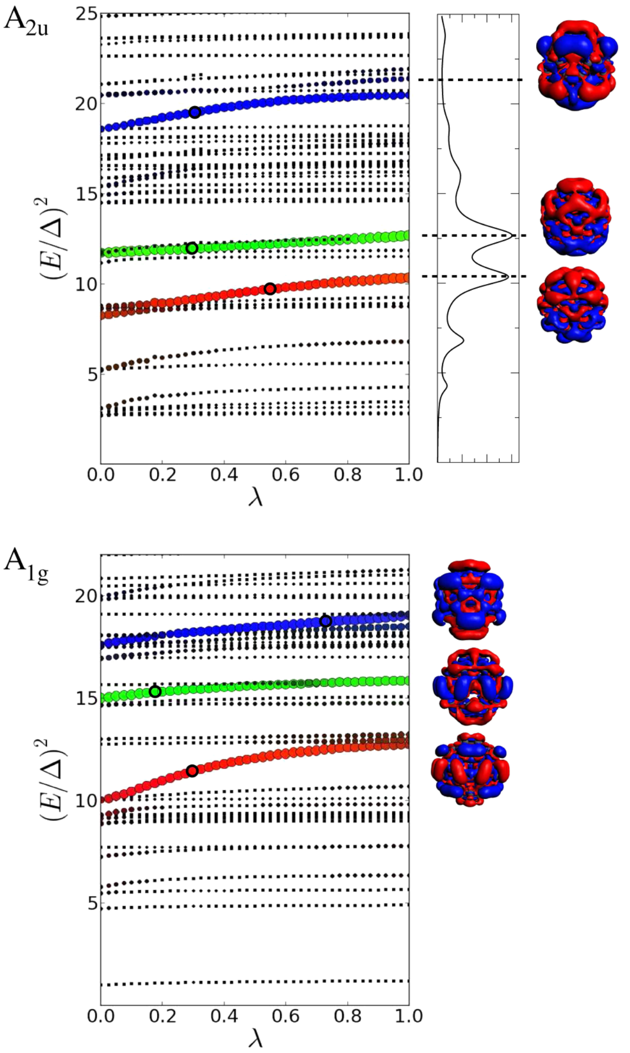

Figure 8. Change of the squared excitation energies of a fullerene C_{60} cluster upon scaling the electronic interaction (left) and isosurface plots of the identified plasmons (right). Excitation energies are plotted in units of the HOMO−LUMO gap (Δ = 1.66 eV) and the coloring scheme described in the text is used to follow the plasmonic excitations, using the excitations highlighted by a black circle as reference points. For dipole-allowed excitations, the linear absorption spectrum is also included.

7. CONCLUSIONS

In this work, we have investigated how plasmonic excitations can be identified in quantum-chemical calculations for molecular systems. To this end, we revisited the three-dimensional electron gas model, where a distinction of single-particle excitations, which correspond to poles of the irreducible response function χ_{irr}, and plasmons, which are due to zeros of the dielectric function ε, emerges naturally. By a step-by-step analysis going from the 3D electron gas over a 1D electron gas to an electron gas in a finite wire, we demonstrated that this separation is preserved for excitations with small wavevectors q. As a final step, we could show that for a molecular sodium chain, the results of a quantum-chemical calculation can be mapped onto the electron gas model. This demonstrates that in molecular systems a classification of electronic excitations as plasmons or single-particle excitations can still be possible.

To identify plasmons in general molecules, we propose to analyze the excitations by scaling the electron−electron interaction in the response calculation. While single-particle excitations are only slightly affected by this scaling, plasmonic excitations are sensitive to variations in the scaling parameter λ. More specifically, their squared excitation energies should increase linearly with the scaling parameter λ. This approach has been implemented for TDDFT and was applied for molecular chains and clusters. It can be easily incorporated into any quantum-chemical program package.

Depending on the system, a number of different cases can be observed. First, in many cases plasmons and single-particle excitations can be clearly distinguished with our analysis. While for some excitations, identified as plasmons, the squared excitation energy increases linearly with the scaling parameter λ, the energies of most excitations, identified as single-particle excitations, are largely independent of λ. Moreover, the composition of the plasmonic excitations is independent of λ and plasmonic and single-particle excitations do not mix even if they become close in energy. Such a behavior is found for the Na_{20} chain, but also for some of the plasmonic excitations in other systems.

Second, for some molecular systems, such as the considered alkene chain, the identified plasmonic excitations mix with certain single-particle excitations if they become close in energy for a certain value of λ. This shows up in our plots as avoided crossings. In these cases, the coloring scheme applied here turns out to be useful for following the plasmonic excitations. Finally, in some cases a strong mixing of plasmonic excitations and single-particle excitations is observed. This is the case for the plasmon with three nodes in the considered Au_{20} chain. Here, the s−s plasmonic excitation mixes with d−s interband single-particle excitations with the same (approximate) wavevector. Thus, the distinction of plasmons and single-particle excitations breaks down in this case.

With the analysis tool developed here for identifying plasmonic excitations, it becomes possible to investigate the dependence of plasmons in molecular clusters as a function of the cluster size. In particular, it will be interesting to study the minimal size of a molecular system that is required to clearly distinguish plasmons from single-particle excitations and to investigate the transition to the regime in which classical models of plasmons become appropriate.[29] The possibility of identifying specific excitations as plasmons opens the way to directly connecting quantum-chemical calculations to such classical models. We plan to explore these questions in our future work.

The scaling approach introduced here for identifying plasmons is not limited to TDDFT, but can also be applied in combination with wave function based quantum-chemical response methods,[14] such as linear-response coupled cluster theory[59,60] or the algebraic diagrammatic construction (ADC) scheme.[61−63] By doing so, one can overcome the shortcomings of common TDDFT exchange−correlation kernels in the description of charge-transfer excitations.[50,51] If such charge-transfer excitations, referred to as excitons in solid-state physics, are described correctly, our scaling analysis should reveal these as an additional, third class of excitations for which the excitation energy decreases with the scaling parameter λ.

Already in combination with TDDFT, the possibility to identify plasmons will allow for dedicated quantum-chemical studies for applications in plasmonics. One example is the design of molecular metamaterials[64−66] guided by quantum chemistry. Another important area is the coupling of molecules to small nanoclusters, both in optical[67,68] and in Raman spectroscopy.[53,69,70] Here, indentifying the relevant plasmonic excitations is a prerequisite for a quantum-chemical treatment with subsystem approaches.[14,71−73] Moreover, with a method for identifying plasmonic excitations available, it will also become possible to calculate these excitations selectively.[74−76] Finally, the present development will also allow for the parametrization of empirical models for treating plasmons in nanoclusters against full quantum-chemical calculations.[77,78]

8. COMPUTATIONAL DETAILS

All calculations in this work were performed with a locally modified version the ADF program package,[79,80] using the BP86 exchange−correlation functional[81,82] and a triple-ζ basis set with one set of polarization functions (TZP). All molecular structures were optimized with the same computational methodology. For the calculations on the gold chain, scalar-relativistic corrections were included via the zeroth-order regular approximation (ZORA).[83−86] For the preparation of the figures using our coloring scheme, we employed the scripting framework PyADF[87] in combination with the MATPLOTLIB package.[88] The linear absorption spectra included in the figures are plotted by using a Lorentzian line shape for each excitation, with an area proportional to the calculated dipole oscillator strength and a full width at half-maximum of $0.2\hbar\omega/\Delta$.

■ AUTHOR INFORMATION

Corresponding Author

*Tel.: +49 721 608 26444 (F.E.) and +49 721 608 48032 (C.R.J.). Fax: +49 721 608 26468 (F.E.) and +49 721 608 48496 (C.R.J.). E-mail: ferdinand.evers@kit.edu (F.E.) and christoph.jacob@kit.edu (C.R.J.).

Notes

The authors declare no competing financial interest.

■ ACKNOWLEDGMENTS

We thank the DFG-Center for Functional Nanostructures for financial support.

■ REFERENCES

(1) Mayer, K. M.; Hafner, J. H. Localized Surface Plasmon Resonance Sensors. *Chem. Rev.* **2011**, *111*, 3828−3857.

(2) Li, Y.; Jing, C.; Zhang, L.; Long, Y.-T. Resonance scattering particles as biological nanosensors in vitro and in vivo. *Chem. Soc. Rev.* **2012**, *41*, 632.

(3) Swierczewska, M.; Liu, G.; Lee, S.; Chen, X. High-sensitivity nanosensors for biomarker detection. *Chem. Soc. Rev.* **2012**, *41*, 2641.

(4) Schuller, J. A.; Barnard, E. S.; Cai, W.; Jun, Y. C.; White, J. S.; Brongersma, M. L. Plasmonics for extreme light concentration and manipulation. *Nat. Mater.* **2010**, *9*, 193−204.

(5) Atwater, H. A.; Polman, A. Plasmonics for improved photovoltaic devices. *Nat. Mater.* **2010**, *9*, 205−213.

(6) Lezec, H. J.; Dionne, J. A.; Atwater, H. A. Negative Refraction at Visible Frequencies. *Science* **2007**, *316*, 430−432.

(7) Ergin, T.; Stenger, N.; Brenner, P.; Pendry, J. B.; Wegener, M. Three-Dimensional Invisibility Cloak at Optical Wavelengths. *Science* **2010**, *328*, 337−339.

(8) Boltasseva, A.; Atwater, H. A. Low-Loss Plasmonic Metamaterials. *Science* **2011**, *331*, 290−291.

(9) Soukoulis, C. M.; Wegener, M. Past achievements and future challenges in the development of three-dimensional photonic metamaterials. *Nat. Photonics* **2011**, *5*, 523−530.

(10) Morton, S. M.; Silverstein, D. W.; Jensen, L. Theoretical Studies of Plasmonics using Electronic Structure Methods. *Chem. Rev.* **2011**, *111*, 3962−3994.

(11) Grimme, S. In *Reviews in Computational Chemistry*; Lipkowitz, K. B., Larter, R., Cundari, T. R., Eds.; Wiley: Hoboken, NJ, 2004; Vol. *20*; pp 153−218.

(12) Harbach, P. H. P.; Dreuw, A. In *Modeling of Molecular Properties*; Comba, P., Ed.; Wiley: Weinheim, Germany, 2011; pp 29−47.

(13) Gonzáalez, L.; Escudero, D.; Serrano-Andrés, L. Progress and Challenges in the Calculation of Electronic Excited States. *ChemPhysChem* **2012**, *13*, 28−51.

(14) Gomes, A. S. P.; Jacob, Ch. R. Quantum-chemical embedding methods for treating local electronic excitations in complex chemical systems. *Annu. Rep. Prog. Chem., Sect. C: Phys. Chem.* **2012**, *108*, 222.

(15) Jacob, Ch. R.; Reiher, M. Localizing normal modes in large molecules. *J. Chem. Phys.* **2009**, *130*, 084106.

(16) Jacob, Ch. R.; Luber, S.; Reiher, M. Analysis of Secondary Structure Effects on the IR and Raman Spectra of Polypeptides in Terms of Localized Vibrations. *J. Phys. Chem. B* **2009**, *113*, 6558−6573.

(17) Jacob, Ch. R.; Luber, S.; Reiher, M. Understanding the Signatures of Secondary-Structure Elements in Proteins with Raman Optical Activity Spectroscopy. *Chem.—Eur. J.* **2009**, *15*, 13491−13508.

(18) van Leeuwen, R.; Baerends, E. J. Exchange-correlation potential with correct asymptotic behavior. *Phys. Rev. A* **1994**, *49*, 2421−2431.

(19) Schipper, P. R. T.; Gritsenko, O. V.; van Gisbergen, S. J. A.; Baerends, E. J. Molecular calculations of excitation energies and (hyper)polarizabilities with a statistical average of orbital model exchange-correlation potentials. *J. Chem. Phys.* **2000**, *112*, 1344−1352.

(20) Neugebauer, J.; Gritsenko, O.; Baerends, E. J. Assessment of a simple correction for the long-range charge-transfer problem in time-dependent density-functional theory. *J. Chem. Phys.* **2006**, *124*, 214102.

(21) Peach, M. J. G.; Benfield, P.; Helgaker, T.; Tozer, D. J. Excitation energies in density functional theory: An evaluation and a diagnostic test. *J. Chem. Phys.* **2008**, *128*, 044118.

(22) Mahan, G. D. *Many Particle Physics*, 3rd ed.; Springer: New York, NY, 2000.

(23) Fetter, A. L.; Walecka, J. D. *Quantum Theory of Many-Particle Systems*; Dover Publications: Mineola, NY, 2003.

(24) Ashcroft, N. W.; Mermin, N. D. *Solid State Physics*; Brooks Cole: New York, NY, 1976.

(25) Nozieres, P.; Pines, D. *Theory Of Quantum Liquids*; Westview Press: Boulder, CO, 1999.

(26) Kittel, C. *Introduction to Solid State Physics*, 8th ed.; Wiley: New York, NY, 2004.

(27) de Heer, W. A.; Selby, K.; Kresin, V.; Masui, J.; Vollmer, M.; Chatelain, A.; Knight, W. D. Collective dipole oscillations in small sodium clusters. *Phys. Rev. Lett.* **1987**, *59*, 1805−1808.

(28) de Heer, W. A. The physics of simple metal clusters: experimental aspects and simple models. *Rev. Mod. Phys.* **1993**, *65*, 611−676.

(29) Jensen, L. L.; Jensen, L. Electrostatic Interaction Model for the Calculation of the Polarizability of Large Noble Metal Nanoclusters. *J. Phys. Chem. C* **2008**, *112*, 15697−15703.

(30) Cottancin, E.; Celep, G.; Lermé, J.; Pellarin, M.; Huntzinger, J.; Vialle, J.; Broyer, M. Optical Properties of Noble Metal Clusters as a Function of the Size: Comparison between Experiments and a Semi-Quantal Theory. *Theor. Chem. Acc.* **2006**, *116*, 514−523.

(31) Halas, N. J.; Lal, S.; Chang, W.-S.; Link, S.; Nordlander, P. Plasmons in Strongly Coupled Metallic Nanostructures. *Chem. Rev.* **2011**, *111*, 3913−3961.

(32) Aikens, C. M.; Li, S.; Schatz, G. C. From Discrete Electronic States to Plasmons: TDDFT Optical Absorption Properties of Ag *n* (*n* = 10, 20, 35, 56, 84, 120) Tetrahedral Clusters. *J. Phys. Chem. C* **2008**, *112*, 11272−11279.

(33) Bae, G.-T.; Aikens, C. M. Time-Dependent Density Functional Theory Studies of Optical Properties of Ag Nanoparticles: Octahedra, Truncated Octahedra, and Icosahedra. *J. Phys. Chem. C* **2012**, *116*, 10356−10367.

(34) Yan, J.; Gao, S. Plasmon resonances in linear atomic chains: Free-electron behavior and anisotropic screening of d electrons. *Phys. Rev. B* **2008**, *78*, 235413.

(35) Klamroth, T.; Nest, M. Ultrafast electronic excitations of small sodium clusters and the onset of electron thermalization. *Phys. Chem. Chem. Phys.* **2009**, *11*, 349−357.

(36) Nayyar, N.; Turkowski, V.; Rahman, T. S. Optical Generation of Collective Plasmon Modes in Small Gold Chains Induced by Doping Transition-Metal Impurities. *Phys. Rev. Lett.* **2012**, *109*, 157404.

(37) Gao, B.; Ruud, K.; Luo, Y. Plasmon resonances in linear noble-metal chains. *J. Chem. Phys.* **2012**, *137*, 194307−194307−11.

(38) Wang, B.-J.; Xu, Y.; Ke, S.-H. Plasmon excitations in sodium atomic planes: A time-dependent density functional theory study. *J. Chem. Phys.* **2012**, *137*, 054101.

(39) Egri, I. Excitons and plasmons in metals, semiconductors and insulators: A united approach. *Phys. Rep.* **1985**, *119*, 363−402.

(40) Cohen-Tannoudji, C.; Diu, B.; Laloe, F. *Quantum Mechanics*, Vol. 2 ; Wiley: New York, NY, 1978.

(41) Schatz, G. C.; Ratner, M. A. *Quantum Mechanics in Chemistry*; Dover Publications: Mineola, NY, 2002.

(42) Casida, M. E. In *Recent Advances in Density-Functional Methods*; Chong, D. P., Ed.; World Scientific: Singapore, 1995; pp 155−192.

(43) Marques, M.; Ullrich, C.; Nogueira, F.; Rubio, A.; Burke, K.; Gross, E. *Time-Dependent Density Functional Theory; Lecture Notes in Physics*; Springer-Verlag: Heidelberg, Germany, 2006; Vol. *706*.

(44) Furche, F.; Rappoprt, D. In *Computational Photochemistry*; Olivucci, M., Ed.; Computational and Theoretical Chemistry; Elsevier: Amsterdam, The Netherlands, 2005; Vol. *16*; pp 93−128.

(45) Casida, M. E.; Huix-Rotllant, M. Progress in Time-Dependent Density-Functional Theory. *Annu. Rev. Phys. Chem.* **2012**, *63*, 287−323.

(46) Giamarchi, T. *Quantum Physics in One Dimension*; Oxford University Press: Oxford, UK, 2004.

(47) Abramowitz, M.; Stegun, I. A. *Handbook of Mathematical Functions: With Formulas, Graphs, and Mathematical Tables*; Dover Publications: Mineola, NY, 1965.

(48) Yan, J.; Yuan, Z.; Gao, S. End and Central Plasmon Resonances in Linear Atomic Chains. *Phys. Rev. Lett.* **2007**, *98*, 216602.

(49) Neugebauer, J.; Louwerse, M. J.; Baerends, E. J.; Wesolowski, T. A. The merits of the frozen-density embedding scheme to model solvatochromic shifts. *J. Chem. Phys.* **2005**, *122*, 094115.

(50) Dreuw, A.; Weisman, J. L.; Head-Gordon, M. Long-range charge-transfer excited states in time-dependent density functional theory require non-local exchange. *J. Chem. Phys.* **2003**, *119*, 2943−2946.

(51) Dreuw, A.; Head-Gordon, M. Failure of Time-Dependent Density Functional Theory for Long-Range Charge-Transfer Excited States: The Zincbacteriochlorin-Bacteriochlorin and Bacteriochlorophyll-Spheroidene Complexes. *J. Am. Chem. Soc.* **2004**, *126*, 4007−4016.

(52) Lian, K.-Y.; Salek, P.; Jin, M.; Ding, D. Density-functional studies of plasmons in small metal clusters. *J. Chem. Phys.* **2009**, *130*, 174701.

(53) Zhao; Jensen, L.; Schatz, G. C. Pyridine-Ag_{20} Cluster: A Model System for Studying Surface-Enhanced Raman Scattering. *J. Am. Chem. Soc.* **2006**, *128*, 2911−2919.

(54) Johnson, H. E.; Aikens, C. M. Electronic Structure and TDDFT Optical Absorption Spectra of Silver Nanorods. *J. Phys. Chem. A* **2009**, *113*, 4445−4450.

(55) Bae, G.-T.; Aikens, C. M. TDDFT and CIS Studies of Optical Properties of Dimers of Silver Tetrahedra. *J. Phys. Chem. A* **2012**, *116*, 8260−8269.

(56) Bertsch, G. F.; Bulgac, A.; Tománek, D.; Wang, Y. Collective plasmon excitations in C_{60} clusters. *Phys. Rev. Lett.* **1991**, *67*, 2690−2693.

(57) Ju, N.; Bulgac, A.; Keller, J. W. Excitation of collective plasmon states in fullerenes. *Phys. Rev. B* **1993**, *48*, 9071−9079.

(58) Bauernschmitt, R.; Ahlrichs, R.; Hennrich, F. H.; Kappes, M. M. Experiment versus Time Dependent Density Functional Theory

Prediction of Fullerene Electronic Absorption. *J. Am. Chem. Soc.* **1998**, *120*, 5052−5059.

(59) Christiansen, O.; Jørgensen, P.; Hättig, C. Response functions from Fourier component variational perturbation theory applied to a time-averaged quasienergy. *Int. J. Quantum Chem.* **1998**, *68*, 1−52.

(60) Christiansen, O.; Halkier, A.; Koch, H.; Jørgensen, P.; Helgaker, T. Integral-direct coupled cluster calculations of frequency-dependent polarizabilities, transition probabilities and excited-state properties. *J. Chem. Phys.* **1998**, *108*, 2801−2816.

(61) Schirmer, J. Beyond the random-phase approximation: A new approximation scheme for the polarization propagator. *Phys. Rev. A* **1982**, *26*, 2395−2416.

(62) Starcke, J. H.; Wormit, M.; Dreuw, A. Unrestricted algebraic diagrammatic construction scheme of second order for the calculation of excited states of medium-sized and large molecules. *J. Chem. Phys.* **2009**, *130*, 024104.

(63) Dutoi, A. D.; Cederbaum, L. S.; Wormit, M.; Starcke, J. H.; Dreuw, A. Tracing molecular electronic excitation dynamics in real time and space. *J. Chem. Phys.* **2010**, *132*, 144302.

(64) Sarychev, A. K.; Shvets, G.; Shalaev, V. M. Magnetic plasmon resonance. *Phys. Rev. E* **2006**, *73*, 036609.

(65) Zhang, S.; Genov, D. A.; Wang, Y.; Liu, M.; Zhang, X. Plasmon-Induced Transparency in Metamaterials. *Phys. Rev. Lett.* **2008**, *101*, 047401.

(66) Rockstuhl, C.; Lederer, F.; Etrich, C.; Pertsch, T.; Scharf, T. Design of an Artificial Three-Dimensional Composite Metamaterial with Magnetic Resonances in the Visible Range of the Electromagnetic Spectrum. *Phys. Rev. Lett.* **2007**, *99*, 017401.

(67) Juluri, B. K.; Lu, M.; Zheng, Y. B.; Huang, T. J.; Jensen, L. Coupling between Molecular and Plasmonic Resonances: Effect of Molecular Absorbance. *J. Phys. Chem. C* **2009**, *113*, 18499−18503.

(68) Zheng, Y. B.; Juluri, B. K.; Lin Jensen, L.; Ahmed, D.; Lu, M.; Jensen, L.; Huang, T. J. Dynamic Tuning of Plasmon−Exciton Coupling in Arrays of Nanodisk−J-aggregate Complexes. *Adv. Mater.* **2010**, *22*, 3603−3607.

(69) Jensen, L.; Zhao, L. L.; Schatz, G. C. Size-Dependence of the Enhanced Raman Scattering of Pyridine Adsorbed on Ag_n (n = 2−8, 20) Clusters. *J. Phys. Chem. C* **2007**, *111*, 4756−4764.

(70) Saikin, S. K.; Chu, Y.; Rappoport, D.; Crozier, K. B.; Aspuru-Guzik, A. Separation of Electromagnetic and Chemical Contributions to Surface-Enhanced Raman Spectra on Nanoengineered Plasmonic Substrates. *J. Phys. Chem. Lett.* **2010**, *1*, 2740−2746.

(71) Neugebauer, J. Couplings between electronic transitions in a subsystem formulation of time-dependent density functional theory. *J. Chem. Phys.* **2007**, *126*, 134116.

(72) Neugebauer, J. Subsystem-Based Theoretical Spectroscopy of Biomolecules and Biomolecular Assemblies. *ChemPhysChem* **2009**, *10*, 3148−3173.

(73) Neugebauer, J. Chromophore-specific theoretical spectroscopy: From subsystem density functional theory to mode-specific vibrational spectroscopy. *Phys. Rep.* **2010**, *489*, 1−87.

(74) Kovyrshin, A.; Neugebauer, J. State-selective optimization of local excited electronic states in extended systems. *J. Chem. Phys.* **2010**, *133*, 174114.

(75) Kovyrshin, A.; Neugebauer, J. Potential-energy surfaces of local excited states from subsystem- and selective Kohn−Sham-TDDFT. *Chem. Phys.* **2011**, *391*, 147−156.

(76) Kovyrshin, A.; Angelis, F. D.; Neugebauer, J. Selective TDDFT with automatic removal of ghost transitions: application to a perylene-dye-sensitized solar cell model. *Phys. Chem. Chem. Phys.* **2012**, *14*, 8608.

(77) Morton, S. M.; Jensen, L. A discrete interaction model/quantum mechanical method for describing response properties of molecules adsorbed on metal nanoparticles. *J. Chem. Phys.* **2010**, *133*, 074103.

(78) Payton, J. L.; Morton, S. M.; Moore, J. E.; Jensen, L. A discrete interaction model/quantum mechanical method for simulating surface-enhanced Raman spectroscopy. *J. Chem. Phys.* **2012**, *136*, 214103.

(79) Theoretical Chemistry, Vrije Universiteit Amsterdam, ADF, Amsterdam density functional program. URL: http://www.scm.com.

(80) te Velde, G.; Bickelhaupt, F. M.; Baerends, E. J.; Fonseca Guerra, C.; van Gisbergen, S. J. A.; Snijders, J. G.; Ziegler, T. Chemistry with ADF. *J. Comput. Chem.* **2001**, *22*, 931−967.

(81) Becke, A. D. Density-functional exchange-energy approximation with correct asymptotic behavior. *Phys. Rev. A* **1988**, *38*, 3098−3100.

(82) Perdew, J. P. Density-functional approximation for the correlation energy of the inhomogeneous electron gas. *Phys. Rev. B* **1986**, *33*, 8822−8824.

(83) van Lenthe, E.; Baerends, E. J.; Snijders, J. G. Relativistic regular two-component Hamiltonians. *J. Chem. Phys.* **1993**, *99*, 4597−4610.

(84) van Lenthe, E.; Baerends, E. J.; Snijders, J. G. Relativistic total energy using regular approximations. *J. Chem. Phys.* **1994**, *101*, 9783−9792.

(85) van Lenthe, E.; Snijders, J. G.; Baerends, E. J. The zero-order regular approximation for relativistic effect: The effect of spin-orbit coupling in closed shell molecules. *J. Chem. Phys.* **1996**, *105*, 6505−6516.

(86) van Lenthe, E.; Ehlers, A.; Baerends, E.-J. Geometry optimizations in the zero order regular approximation for relativistic effect. *J. Chem. Phys.* **1999**, *110*, 8943−8953.

(87) Jacob, Ch. R.; Beyhan, S. M.; Bulo, R. E.; Gomes, A. S. P.; Götz, A. W.; Kiewisch, K.; Sikkema, J.; Visscher, L. PyADF — A scripting framework for multiscale quantum chemistry. *J. Comput. Chem.* **2011**, *32*, 2328−2338.

(88) MATHPLOTLIB — A Python 2D plotting library. URL: http://matplotlib.sourceforge.net/.